Monthly Notices of the ROYAL ASTRONOMICAL SOCIETY

MNRAS **544,** 548–571 (2025) https://doi.org/10.1093/mnras/staf1574
Advance Access publication 2025 September 17

GRB 241105A: a test case for GRB classification and rapid *r*-process nucleosynthesis channels

Dimple,[1,2]★ B. P. Gompertz ,[1,2] A. J. Levan,[3] D. B. Malesani,[3] T. Laskar,[3,4] S. Bala,[5] A. A. Chrimes ,[3,6] K. Heintz ,[7] L. Izzo,[8] G. P. Lamb ,[9] D. O'Neill,[1,2] J. T. Palmerio ,[10] A. Saccardi,[10] G. E. Anderson ,[11] C. De Barra,[12] Y. Huang,[13] A. Kumar ,[14] H. Li,[15] S. McBreen,[12] O. Mukherjee,[5] S. R. Oates ,[16] U. Pathak,[17] Y. Qiu,[15] O. J. Roberts ,[5] R. Sonawane,[18,19] P. Veres,[20] K. Ackley,[21] X. Han,[15] Y. Julakanti,[21] J. Wang,[15] P. D'Avanzo,[22] A. Martin-Carrillo,[12] M. E. Ravasio,[3,22] A. Rossi ,[23] N. R. Tanvir,[24] J. P. Anderson,[25,26] M. Arabsalmani,[27,28] S. Belkin ,[29] R. P. Breton ,[30] R. Brivio,[22] E. Burns,[31] J. Casares ,[32,33] S. Campana,[22] S. I. Chastain ,[34] V. D'Elia,[35] V. S. Dhillon ,[32,36] M. J. Dyer ,[36] J. P. U. Fynbo,[7] D. K. Galloway,[29] A. Gulati ,[37,38,39] B. Godson,[21] A. J. Goodwin ,[11] M. Gromadzki,[40] D. H. Hartmann,[41] P. Jakobsson,[42] T. L. Killestein,[21] R. Kotak,[43] J. K. Leung,[44,45,46] J. D. Lyman ,[21] A. Melandri,[47] S. Mattila,[43,48] S. McGee,[1,2] C. Morley,[11] T. Mukherjee,[49,50] T. E. Müller-Bravo,[51,52] K. Noysena,[53] L. K. Nuttall,[54] P. O'Brien,[24] M. De Pasquale,[55] G. Pignata,[56] D. Pollacco,[21] G. Pugliese,[57] G. Ramsay,[58] A. Sahu,[21] R. Salvaterra,[59] P. Schady ,[60] B. Schneider,[61] D. Steeghs ,[21] R. L. C. Starling ,[24] K. Tsalapatas,[62] K. Ulaczyk,[21] A. J. van der Horst,[63] C. Wang,[13,64] K. Wiersema,[65] I. Worssam,[1,2] M. E. Wortley,[1,2] S. Xiong[13] and T. Zafar [49]

Affiliations are listed at the end of the paper

Accepted 2025 September 13. Received 2025 September 8; in original form 2025 July 21

ABSTRACT

Gamma-ray bursts (GRBs) offer a powerful window to probe the progenitor systems responsible for the formation of heavy elements through the rapid neutron capture (*r*-) process, thanks to their exceptional luminosity, which allows them to be observed across vast cosmic distances. GRB 241105A, observed at a redshift of $z = 2.681$, features a short initial spike ($\sim$1.5 s) and a prolonged weak emission lasting about 64 s, positioning it as a candidate for a compact binary merger and potentially marking it as the most distant merger-driven GRB observed to date. However, the emerging ambiguity in GRB classification necessitates further investigation into the burst's true nature. Prompt emission analyses, such as hardness ratio, spectral lag, and minimum variability time-scales, yield mixed classifications, while machine-learning-based clustering places GRB 241105A near both long-duration mergers and collapsar GRBs. We conducted observations using the *James Webb Space Telescope* (*JWST*) to search for a potential supernova counterpart. Although no conclusive evidence was found for a supernova, the host galaxy's properties derived from the *JWST* observations suggest active star formation with low metallicity, and a sub-kpc offset of the afterglow from the host, which appears broadly consistent with a collapsar origin. Nevertheless, a compact binary merger origin cannot be ruled out, as the burst may plausibly arise from a fast progenitor channel. This would have important implications for heavy element enrichment in the early Universe.

Key words: gamma-ray burst: individual: GRB 241105A – gamma-ray bursts.

1 INTRODUCTION

Gamma-ray bursts (GRBs) are the most powerful explosions in the universe, releasing an enormous amount of energy in a short period. Historically, GRBs have been divided into two observational classes. Those with durations of up to two seconds (termed 'short' GRBs) are thought to be powered by neutron star mergers, while those with longer durations ('long' GRBs) come from the collapse of very massive stars (Kouveliotou et al. 1993, see also Zhang & Mészáros 2004; Zhang et al. 2006, 2009; Zhang 2014). However, the limitations of this framework have been recognized over time (Fynbo et al. 2006; Gehrels et al. 2006; Zhang et al. 2009; Dimple et al. 2022a). Recent advances have shown that this duration-based division does not cleanly separate mergers from collapsars. In particular, the discovery of kilonovae accompanying GRBs 211211A (Mei et al.

★ E-mail: d.dimple@bham.ac.uk

2022; Rastinejad et al. 2022; Troja et al. 2022; Yang et al. 2022) and 230307A (Gillanders et al. 2023; Levan et al. 2024; Yang et al. 2024), both with durations of ~ 30 s, has changed the canonical classification scheme. Such long-lasting merger-powered GRBs are incompatible with the short accretion time-scale expected under the standard assumption that the merging neutron star binary promptly collapses to a black hole, and may indicate the need for additional physics-like magnetic field effects (Proga & Zhang 2006; Gottlieb et al. 2023), a longer-lasting central engine (Metzger et al. 2011; Bucciantini et al. 2012; Gompertz et al. 2013; Rowlinson et al. 2013; Gompertz, O'Brien & Wynn 2014), or the merger of a neutron star–black hole binary system (e.g. Desai, Metzger & Foucart 2019; Gompertz, Levan & Tanvir 2020; Dimple, Misra & Arun 2023).

The current classification uncertainty has intensified interest in methods to reliably separate GRBs powered by collapsing stars from those powered by merging compact objects based on the prompt gamma-ray emission. Potential diagnostic properties include apparently distinct correlations between the isotropic equivalent energy emitted in gamma-rays ($E_{\rm iso}$) and the peak spectral energy (E_p; the 'Amati relation;' Amati et al. 2002; Amati 2006; Minaev & Pozanenko 2020); non-zero lags in the arrival times of soft gamma-ray photons relative to hard ones in collapsar GRBs (Norris 2002); and disparate minimum variability time-scales (MVTs) between the two engine types (MacLachlan et al. 2013) which may probe the size of the emission region. Lately, efforts have turned to classifications based on machine learning (ML) techniques (Chattopadhyay & Maitra 2017; Acuner & Ryde 2018; Jespersen et al. 2020; Salmon, Hanlon & Martin-Carrillo 2022; Dimple et al. 2023, 2024b; Steinhardt et al. 2023; Mehta & Iyyani 2024; Zhu et al. 2024). The application of unsupervised ML algorithms on prompt emission light curves observed by the Burst Alert Telescope (BAT; Barthelmy et al. 2005a) on the *Neil Gehrels Swift Observatory* (*Swift;* Gehrels et al. 2004) and the Gamma-ray Burst Monitor (GBM, Meegan et al. 2009) onboard the *Fermi* spacecraft, revealed multiple clusters within the GRB population, suggesting the tantalizing possibility that some clusters correspond to specific progenitor types.

Ultimately, measurements that can definitively identify the progenitor type will be required to verify the robustness of any prompt emission-based classification schemes. For collapsars, this is the identification of a supernova (SN, e.g. Galama et al. 1998; Hjorth et al. 2003; Stanek et al. 2003), the smoking gun of a collapsing star. Recent examples of this include the identification of SNe accompanying the nominally short GRB 200826A (Ahumada et al. 2021; Zhang et al. 2021; Rossi et al. 2022), the shortest known collapsar event; the unusually soft GRB 201015A (Patel et al. 2023; Belkin et al. 2024); and the Fast X-ray Transient (FXT) EP240414a (van Dalen et al. 2025), whose broad-lined Type Ic SN links it to GRB progenitor stars. For mergers, positive confirmation can come in the form of accompanying gravitational wave (GW) radiations (Abbott et al. 2017) or kilonovae (Berger, Fong & Chornock 2013; Tanvir et al. 2013; Jin et al. 2015, 2016, 2018, 2020; Yang et al. 2015; Kasliwal et al. 2017; Villar et al. 2017; Gompertz et al. 2018; Troja et al. 2018, 2019, 2022; Eyles et al. 2019; Lamb et al. 2019; Fong et al. 2021; O'Connor et al. 2021; Mei et al. 2022; Yang et al. 2022, 2024; Levan et al. 2024), but also from the definitive exclusion of SNe. A recent notable example of this was GRB 191019A, which may be the first example of a merger formed through dynamical capture (Levan et al. 2023; Stratta et al. 2025), possibly in the accretion disc of an active galactic nucleus (Lazzati et al. 2023).

Historically, the exclusion of an SN associated with the nearby ($z = 0.125$) long GRB 060 614 to limits $100\times$ fainter than any previously known example (Fynbo et al. 2006; Gal-Yam et al. 2006; Gehrels et al. 2006) led to the recognition of the subpopulation of so-called extended emission (EE) GRBs, of which 211211A and 230307A are members (Gompertz et al. 2023). EE events are characterized by short, hard 'spikes' of gamma-ray emission with typical durations of less than two seconds, followed by lower luminosity and spectrally softer gamma-ray emission that can last for tens to hundreds of seconds (Norris & Bonnell 2006; Norris, Gehrels & Scargle 2010). The initial spikes are well matched to classic short GRBs, while the formal duration of EE GRBs extends well into the long GRB range. The ratio of the energy contained in the spike and the EE has been shown to be highly variable (Perley et al. 2009), suggesting a continuum running from short GRBs with no EE through to rare examples of EE-dominated events like GRBs 080 503 (Perley et al. 2009) and 191019A (Levan et al. 2023; Stratta et al. 2025). EE is often attributed to the spin-down of a newly formed magnetar (Metzger et al. 2011; Bucciantini et al. 2012; Gompertz et al. 2013; Gompertz et al. 2014) or fallback accretion processes (e.g. Rosswog 2007), potentially due to a neutron star–black hole binary system (Troja et al. 2008; Desai et al. 2019; Gompertz et al. 2020).

GRB 241105A, detected at a redshift of $z = 2.681$ (Izzo et al. 2024), emerges as a pivotal case in this evolving paradigm. Its light-curve morphology, with an initial hard spike lasting ~ 1.5 s followed by weaker emission extending to ~ 64 s (The Fermi GBM team 2024), is consistent with a short GRB with potential EE, positioning it as a candidate for a compact binary merger (DeLaunay et al. 2024; The Fermi GBM team 2024). If confirmed as a merger-driven event, GRB 241105A would be the most distant such GRB observed to date, offering a unique probe of neutron star merger rates in the early Universe. This is particularly significant for understanding *r*-process nucleosynthesis, as standard merger models predict long delay times (hundreds of millions of years) that challenge their ability to enrich the early Universe with heavy elements (Hotokezaka, Beniamini & Piran 2018; Côté et al. 2019; Skinner & Wise 2024). Confirming GRB 241105A as a higher redshift merger could support models for rapid binary evolution or strong natal kicks, enabling faster merger channels (Belczynski, Kalogera & Bulik 2002; Belczynski et al. 2006; O'Shaughnessy, Belczynski & Kalogera 2008; Tauris et al. 2013; Beniamini & Piran 2019). As such, it would provide crucial observational evidence for the rapid production of heavy elements, representing a significant step toward solving the long-standing puzzle of chemical enrichment in the early Universe. Conversely, identifying it as a collapsar would cast further doubt on EE-like phenomenology as a reliable discriminant of progenitor type, deepening the GRB classification crisis. In both scenarios, this burst serves as a critical test case for GRB classification and rapid channels for *r*-process nucleosynthesis, making its study essential for advancing our understanding of GRB progenitors.

In this paper, we perform a multiwavelength study of GRB 241105Ato probe its origin. The structure of this paper is as follows. In Section 2, we present multiwavelength observations and data analysis of GRB 241105A. Section 3 examines the prompt emission characteristics of the burst. Section 4 presents the afterglow modelling using multiband data. Section 5 discusses the properties of the host galaxy, including SED fitting and afterglow offset analysis based on the *James Webb Space Telescope* (*JWST*) imaging. Finally, in Section 6, we discuss the progenitor scenario for the burst based on its prompt, afterglow and host properties. We assume a flat universe ($\Omega_{\rm k} = 0$) with the cosmological parameters $H_0 = 70$ km s^{-1} Mpc^{-1}, and the density parameters $\Omega_\Lambda = 0.7$, and $\Omega_{\rm m} = 0.3$.

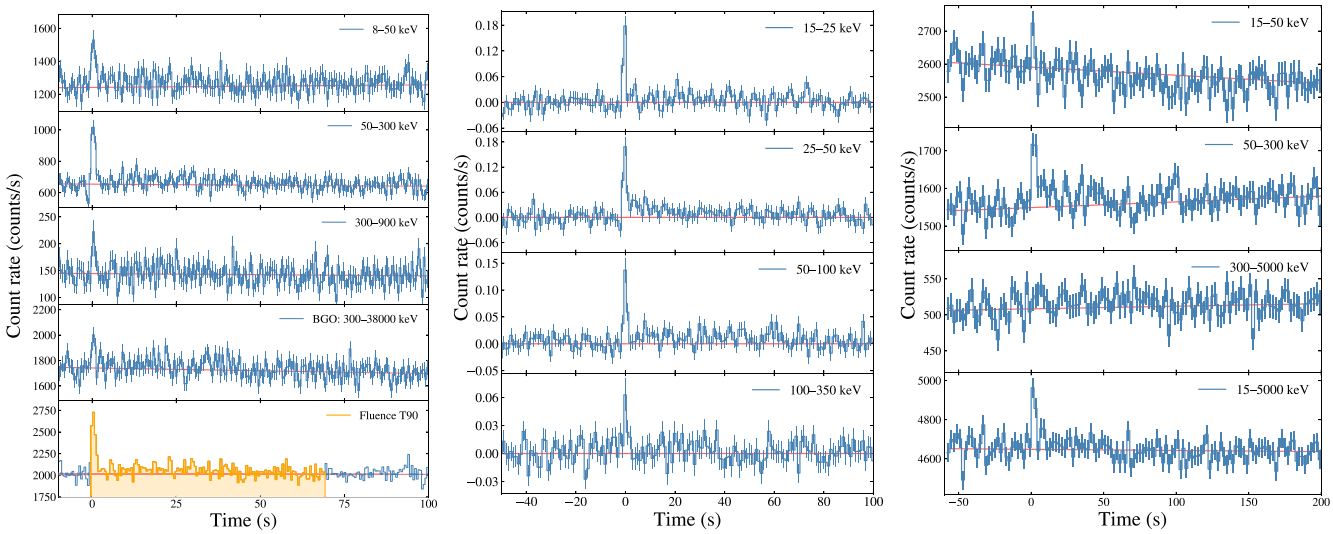

Figure 1. Light curves of GRB 241105A as detected by *Fermi*/GBM(left), *Swift*/BAT(middle), and *SVOM*/GRM (right) in different energy bands. The red lines are the fitted background. The bottom panel in the GBM plot (left) shows T_{90} of 69.0 s overlaid on the combined NaI light curve in the 8–900 keV range.

2 OBSERVATIONS AND DATA REDUCTION

GRB 241105Atriggered the *Fermi*/GBM flight software at 16:06:04.66 UTC (T_0), 752515569 MET (trigger id: bn 241105671), and was identified as a short burst featuring a short spike followed by a weak EE. *Fermi*/GBM distributed an automated localization through the General Coordinates Network. The burst was also detected by *Swift*/BAT (DeLaunay et al. 2024), Konus-Wind (Frederiks et al. 2024), and *SVOM* (Space-based multiband astronomical Variable Objects Monitor)/GRM (SVOM/GRM Team 2024), with all missions confirming the presence of the weak emission following the main burst. The burst triggered an extensive multiwavelength campaign spanning gamma-ray, ultraviolet (UV), optical, near-infrared (NIR), and radio wavelengths. This section outlines the observational data collected across these bands and the methodologies employed to analyse the event.

2.1 High-energy observations

2.1.1 Fermi*/GBM*

We extracted the time-tagged event (TTE) data for the event, and performed analysis using the `GBM Data Tools`,[1] PYTHON library (Goldstein, Cleveland & Kocevski 2023). The left panel of Fig. 1 shows the combined *Fermi*/GBM light curve for the Sodium–Iodide (NaI) detectors Na and Nb, along with the B1 Bismuth–Germanate (BGO) detector, which detects higher energy photons up to 40 MeV. The 2 NaI detectors were combined based on their source angle relative to the burst. Due to the relationship between detector effective area and source angle (Bissaldi et al. 2009), detectors with source angles $\gtrsim 60^\circ$ are typically not used in temporal and spectral analyses. The burst also triggered detector N6. However, this detector would have been occulted by the spacecraft, and the initial pulse is not visible in the TTEs. Therefore, it is not included here. The background in the surrounding intervals was fit with a first-order polynomial and is shown in red in the left panel of Fig. 1. We estimated the T_{90} for the burst using the GBM TTE and RMFIT[2] software, in the 50–300 keV band. The T_{90} duration is 69.0 ± 13.5 s, placing it well into the regime of long-duration GRBs. However, this duration includes a short, initial hard spike lasting $\sim$1.5 s, followed by a prolonged weaker emission of around $\sim$64 s. We divided the event in two emission episodes; episode 1 from $T_0 - 0.256$ to $T_0 + 1.28$ s and episode 2 from $T_0 + 1.28$ to $T_0 + 69.0$ s. We extracted the spectra for these two episodes using `GBM Data Tools`. For this, we used the TTE data in the energy channels in the range of 8–900 keV for NaI detectors (Na and Nb) and 0.3–35 MeV for BGO detectors (B1).

2.1.2 Swift*/BAT*

Swift/BAT did not trigger on GRB 241105A in real time. However, the *Fermi* notice triggered the Gamma-ray Urgent Archiver for Novel Opportunities (Tohuvavohu et al. 2020), which prompted the BAT event data between $T_0 - 50$ and $T_0 + 150$ s to be saved and delivered to the ground. Ground analysis of these data revealed a detection of the GRB (see DeLaunay et al. 2024).

BAT data were downloaded from the UK Swift Science Data Centre (UKSSDC; Evans et al. 2007, 2009). Per the header information in the event file, a *Swift* clock correction of -34.4815s was applied to the photon arrival times to make them consistent with the data from the other high-energy satellites. The event data were processed using the standard High Energy Astrophysics Software (HEASOFT; Nasa High Energy Astrophysics Science Archive Research Center (HEASARC) 2014) tools to apply mask weighting and a ray tracing solution. Spectra were created with the BATBINEVT routine, and response matrices with the BATDRMGEN script. The *Swift*/BAT light curve of GRB 241105A is shown in the middle panel of Fig. 1.

2.1.3 SVOM*/GRM*

The *SVOM* (Cordier et al. 2015; Wei et al. 2016; Atteia, Cordier & Wei 2022) carries two wide-field high-energy instruments: a coded-mask gamma-ray imager (the ECLAIRs; Godet et al. 2014) and a Gamma-Ray Monitor (GRM; Dong et al. 2010; Wen et al. 2021); and two narrow-field telescopes: a Microchannel X-ray Telescope (Götz et al. 2023), and a Visible-band Telescope (VT; Fan et al. 2020).

[1] https://fermi.gsfc.nasa.gov/ssc/data/analysis/gbm/
[2] https://fermi.gsfc.nasa.gov/ssc/data/analysis/rmfit

Table 1. Photometric observations of the afterglow of GRB 241105A. Magnitudes are in the AB system and are not corrected for Galactic extinction.

Δt (h)	Filter	Magnitude (AB)	Telescope
0.48	*L*	17.21 ± 0.01	GOTO
9.90	*r*	19.20 ± 0.20	BOOTES-7[a]
11.08	*R*	19.51 ± 0.02	VLT/FORS2
14.36	*R*	19.88 ± 0.03	SVOM/VT
16.04	*R*	20.22 ± 0.03	SVOM/VT
17.72	*R*	20.68 ± 0.04	SVOM/VT
19.37	*R*	20.84 ± 0.05	SVOM/VT
35.50	*r*	22.66 ± 0.10	ePESSTO + NTT
51.76	*R*	22.33 ± 0.15	SVOM/VT
14.36	*B*	20.79 ± 0.05	SVOM/VT
16.04	*B*	21.21 ± 0.06	SVOM/VT
17.72	*B*	21.57 ± 0.07	SVOM/VT
19.37	*B*	21.52 ± 0.06	SVOM/VT
51.76	*B*	> 23.7	SVOM/VT
14.68	White	$22.24^{+0.11}_{-0.10}$	*Swift*/UVOT
16.84	*o*	19.65 ± 0.14	ATLAS
27.40	White	$23.73^{+0.53}_{-0.36}$	*Swift*/UVOT
35.61	*z*	22.88 ± 0.25	ePESSTO + NTT
68.44	*L*	> 19.81	GOTO

Note. [a]Hu et al. (2024).

SVOM/GRM was triggered in-flight by GRB 241105A (*SVOM* burst-id: sb24110502) at 2024-11-05T16:06:05 UT by individual GRM detectors GRD01 and GRD03 (SVOM/GRM Team 2024). The energy of GRM event data were calibrated using the GRM CALDB.[3] The right panel of Fig. 1 shows the *SVOM*/GRM light curve combined with all three GRDs in different energy bands. It shows that the burst consists of a short single pulse with a duration of about 2 s and a weaker EE with a duration of about 50 s. The spectra were created within the same time intervals as *Fermi*/GBM. The background of *SVOM*/GRM is estimated by fitting the data from $T_0 - 50$ to $T_0 - 10$ s and $T_0 + 150$ to $T_0 + 200$ s with first-order polynomials. The response matrices were created from GRM CALDB. A joint gamma-ray spectral analysis incorporating *SVOM*/GRM, *Fermi*/GBM, and *Swift*/BAT is performed later in Section 3.1.

2.2 Optical/UV observations

Photometric and spectroscopic follow-up of GRB 241105A was conducted across multiple facilities and filters, with observations spanning the ultraviolet to IR wavelengths. All measured magnitudes and upper limits are compiled in Table 1.

2.2.1 *GOTO afterglow discovery*

The Gravitational-wave Optical Transient Observer (GOTO, Dyer et al. 2020, 2024; Steeghs et al. 2022) responded autonomously (Dyer 2020) to the *Fermi* GCN notice (The Fermi GBM team 2024) from its southern site at Siding Spring Observatory in New South Wales, Australia. Across 10 unique pointings, GOTO-South tiled 277.9 deg^2 within the *Fermi*/GBM 90 per cent localization region between 2024-11-05 16:19:10 UT (+0.22 h post-trigger) to 2024-11-05 17:42:50 UT (+ 1.61 h post-trigger), achieving a total coverage of 84.3 per cent of the 2D localization probability. Each pointing consisted of 4 × 90 s exposures in GOTO *L* band (400–700 nm). Over the course of this imaging campaign, 104 images were captured with an average 5-sigma depth of $L = 20.4$ mag.

The data were processed promptly upon acquisition using the GOTO pipeline (Lyman et al. in preparation), incorporating difference imaging against deeper template observations of the same pointings to identify transient sources. An automated ML classifier (Killestein et al. 2021) was employed to initially filter source candidates, which were subsequently cross-matched with contextual and minor planet catalogs to eliminate false positives. Any candidates passing these automated checks underwent real-time human vetting, ensuring rigorous verification of potential transient events.

After filtering out galactic variables and other false positives, a new optical source (internal name GOTO24ibf; IAU designation AT 2024aaon) was identified in images taken at 2024-11-05 16:34:35 (+ 0.48 h post-trigger) at J2000 coordinates $\alpha = 04^{\rm h}24^{\rm m}59.00^{\rm s}$, $\delta = -49^\circ45'09.33''$ (Julakanti et al. 2024). The source was not present in earlier GOTO observations taken on 2024-11-05 at 10:48:54 UT, 5.29 h before the GRB trigger, with a 3σ limiting magnitude of $L > 20.6$ (see Fig. 2). Furthermore, no evidence of the source was found in archival data from the Asteroid Terrestrial-impact Last Alert System (ATLAS; Tonry et al. 2018a) forced photometry server (Shingles et al. 2021), supporting its classification as a new transient source. The GOTO discovery refined the localization precision of GRB 241105A from hundreds of square degrees to sub-arcsecond, enabling subsequent multiwavelength observations that ultimately confirmed GOTO24ibf/AT 2024aaon as the afterglow (Dichiara et al. 2024; Hu et al. 2024; Kennea et al. 2024; Qui et al. 2024; Rastinejad et al. 2024; Siegel et al. 2024; Tsalapatas et al. 2024; Izzo et al. 2024; Anderson et al. 2024c). Magnitudes and upper limits in the GOTO *L* band were derived using forced photometry performed through the GOTO Lightcurve Service (Jarvis et al. in preparation).

2.2.2 *VLT/FORS2 spectroscopy and redshift determination*

We observed the optical counterpart (Julakanti et al. 2024) of GRB 241105A using the FOcal Reducer and low-dispersion Spectrograph (FORS2) mounted on the Very Large Telescope (VLT) Unit Telescope 1 (UT1; Antu, Appenzeller et al. 1998). The instrument was equipped with grisms 300V (without an order-sorting filter) and 300I (with the OG590 filter). We started observations on 2024 November 06 at 03:11:31 UT with an exposure time of 600 s per grism. The optical counterpart was clearly detected in the acquisition image (Izzo et al. 2024). The magnitude is calibrated using the SkyMapper catalogue and is tabulated in Table 1.

The spectral data were reduced using standard procedures. The final combined spectrum is shown in Fig. 3. A continuum is detected over the entire wavelength range from 3500 to 10 000 Å and a trough due to Lyα absorption is visible at the blue end. We identify several metal absorption features such as S II, Si II, Si II*, O I, C II, C II*, Fe II, Al II, N V, C IV, Si IV, and Al III. The line profiles of low-ionization transitions show a single strong component centred at $z = 2.681$ (see Fig. 3). High-ionization absorption lines also show only one component but blueshifted by ~ -150 km s^{-1}. Further details on the absorption lines analysis are discussed in Section 5 and Appendix B. With a secure spectroscopic redshift of $z = 2.681$, GRB 241105A may represent the most distant short GRB known to date; if its origin is confirmed to be a neutron star merger, it would be the farthest such event yet discovered, significantly extending the redshift frontier for compact-binary merger-driven GRBs.

[3]https://grm.ihep.ac.cn/CALDB.jhtml

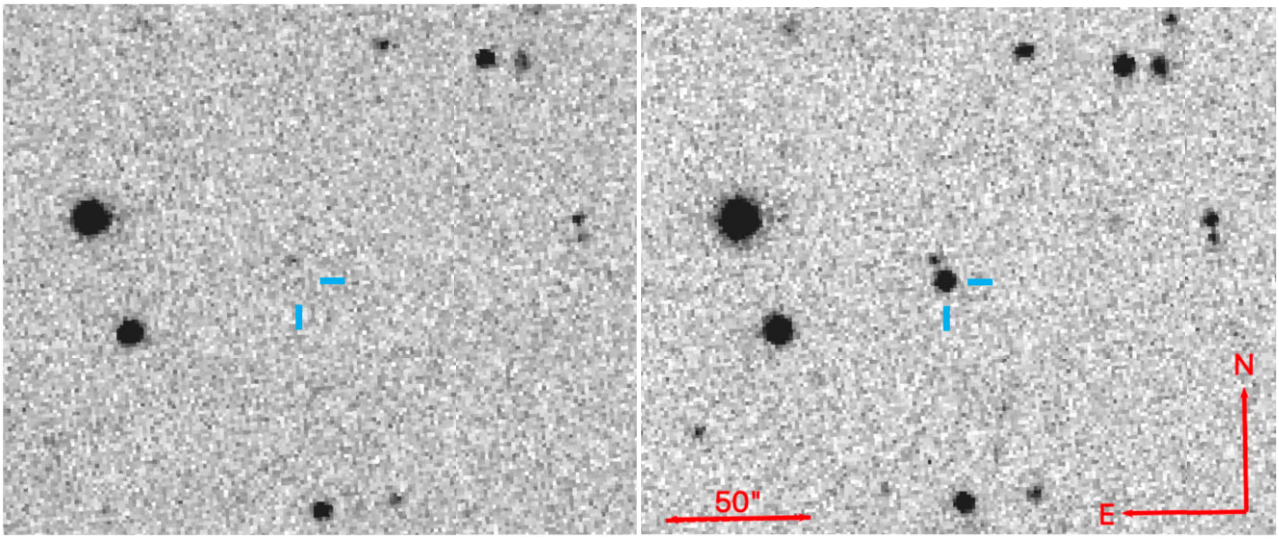

Figure 2. Left: a pre-trigger GOTO image of the field taken as part of the all-sky survey at 10:48:54 UT (T_0−5.29 h), showing no source at the afterglow position. Right: the GOTO discovery image of the afterglow of GRB 241105A, taken at 16:34:35 UT on 2024 November 05 (T_0 + 0.48 h), shows the transient marked at the burst location.

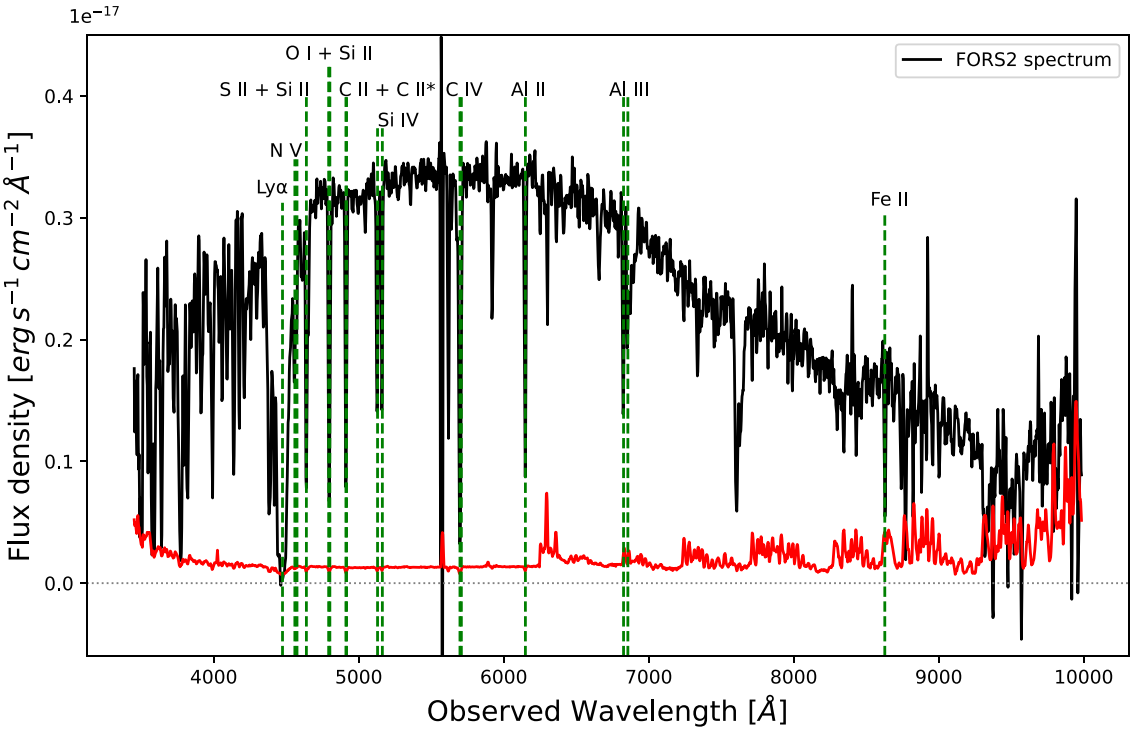

Figure 3. VLT/FORS2 optical afterglow spectrum of GRB 241105A at redshift $z = 2.681$. Data are in black, the error spectrum is in red, and the horizontal dotted line in grey corresponds to $F_\lambda = 0$. The green vertical lines correspond to the labelled absorption lines.

2.2.3 NTT

The advanced Public ESO Spectroscopic Survey for Transient Objects (ePESSTO + ; Smartt et al. 2015) started observing the field of GRB241105A with the ESO New Technology Telescope (NTT) at La Silla, equipped with the ESO Faint Object Spectrograph and Camera 2 (EFOSC2), in imaging mode. Observations started on 2024 November 07 at 03:21:27 UT, using the r and z Gunn filters. The r and z images consisted of five exposures of 180 s each. The z-band images were dithered to enable the fringing correction prior to alignment and stacking using a 2×2 re-binned ESO NTT-EFOSC2 fringing mask provided by ESO.[4] Magnitudes were calibrated against the ATLAS-REFCAT2 catalogue (Tonry et al. 2018b). The afterglow was clearly detected in r and z bands (Tsalapatas et al. 2024), and the magnitudes are reported in Table 1.

[4]https://www.eso.org/sci/facilities/lasilla/instruments/efosc/inst/fringing.html

2.2.4 SVOM*/VT*

SVOM/VT has an effective aperture of 43 cm and a field of view of 26×26 arcmin^2, giving a pixel scale of 0.76 arcsec. It conducts observations with two channels, VT_B and VT_R, simultaneously, covering wavelengths of 400–650 and 650–1000 nm, respectively. Detailed information on VT will be presented in Qiu et al. (in preparation). During the commissioning phase, VT observed GRB 241105A using the target-of-opportunity (ToO) mode on 2024 November 06 and 07. Five orbits covering 7 h were scheduled with the earliest observation starting on 2024 November 06, about 14.2 h post-trigger time. The counterpart was clearly detected in all stacked images in each orbit (Qui et al. 2024). On 2024 November 07, the counterpart was marginally detected in *R*-band stacked images at about 51.7 h post-trigger time and undetected in *B*-band stacked images with a total exposure time of 6800 s. For all observations, individual exposures were set to 20 s per frame. All data were processed in a standard manner, including zero correction, dark correction, and flat-field correction. After pre-processing, the images for each band obtained during each observation were stacked to increase the signal-to-noise ratio. Photometric measurements, calibrated in the AB magnitude system, are presented in Table 1.

2.2.5 Swift/UVOT

The *Swift*/Ultra-Violet and Optical Telescope (UVOT, Roming et al. 2005) began observations of the field of GRB 241105A around 10.6 h after the *Fermi*/GBM trigger (Siegel et al. 2024). Observations were taken with the *white* filter only. A faint fading source was detected at the afterglow position (Siegel et al. 2024). Source counts were extracted from the UVOT image mode data using a source region of 5 arcsec radius. Background counts were extracted using four circular regions of radius 10 arcsec located in source-free regions near the GRB. The count rates were obtained from the co-added images using the *Swift* tool `uvotsource`. They were converted to magnitudes using the UVOT photometric zero-points (Poole et al. 2008; Breeveld et al. 2011).

2.3 *JWST* observations

We conducted ToO observations with JWST under Director's Discretionary Time (ID: 9228, PI: Dimple). Observations were taken with the Near InfraRed Camera (NIRCam; Rieke et al. 2023) in six wide filters (*F*070*W*, *F*115*W*, *F*150*W*, *F*277*W*, *F*356*W*, and *F*444*W*), beginning on 2024 December 22 at 17:26:00 UT – approximately 47 d after the burst ($\sim$ 12.7 d in the GRB rest frame), close to the predicted observer-frame peak of any accompanying SN (e.g. Galama et al. 1998; Patat et al. 2001). We detected a galaxy in all the observed bands, which archival images (Julakanti et al. 2024) had previously identified. The galaxy was resolved into at least two distinct extended regions separated by $\sim$ 0.2 arcsec, as shown in Fig. 4. We performed photometric analysis in a 0.1 arcsec aperture at the afterglow location. We obtained a magnitude of *F*277*W*(AB)$= 23.87 \pm 0.001$, approximately 2.4 mag brighter than the anticipated SN 1998bw-like peak, which makes host subtraction essential to reveal any transient. In addition, we performed photometric analysis for the complete galaxy, which was later used for the host analysis. All photometric measurements are reported in Table 2.

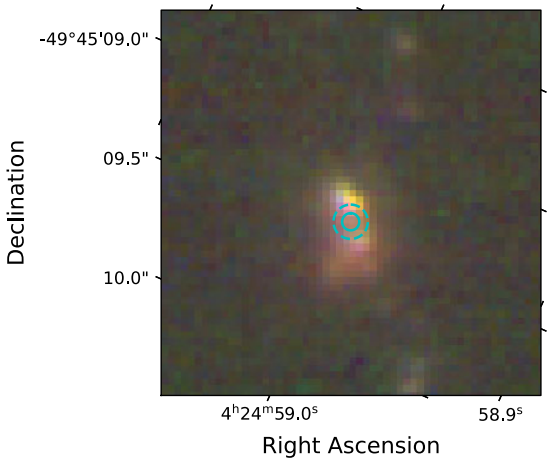

Figure 4. The position of GRB241105A overlaid on a composite *JWST* NIRCam image combining filters *F*070*W*, *F*115*W*, and *F*150*W*, as described in Section 5.3. The disturbed/irregular morphology of the host is clearly visible. 1σ (solid circle, 36 mas) and 2σ (dashed circle, 72 mas) uncertainties on the transient position are shown.

Table 2. *JWST*/NIRCam AB magnitudes of the host galaxy of GRB 241105A measured in two apertures.

Filter	0.1 arcsec aperture (mag)	1 arcsec aperture (mag)
*F*070*W*	24.52 ± 0.006	23.28 ± 0.15
*F*115*W*	24.30 ± 0.004	23.14 ± 0.05
*F*150*W*	24.89 ± 0.005	22.87 ± 0.05
*F*277*W*	23.87 ± 0.001	22.54 ± 0.03
*F*356*W*	24.06 ± 0.002	22.67 ± 0.04
*F*444*W*	23.73 ± 0.002	22.54 ± 0.03

2.4 Radio observations

2.4.1 ATCA

Observations with the Australia Telescope Compact Array (ATCA) 4 cm dual receiver (central frequencies of 5.5 and 9 GHz both with a 2 GHz bandwidth) commenced 4.8 d post-burst under program C3204 (PI: Anderson). Following the standard techniques, the data were processed using MIRIAD (Sault, Teuben & Wright 1995) with PKS 1934−638 and PKS 0437−454 as the primary and gain calibrator, respectively. While no radio counterpart was detected during this first epoch (Anderson et al. 2024b), a follow-up observation 15 d post-burst detected the afterglow at 9 GHz (Anderson et al. 2024c). We then performed higher frequency follow-up with the 15 mm dual receiver (central frequencies of 17 and 19 GHz) at 17 d post-burst, which was combined in the visibility plane to obtain a detection at 18 GHz. A further observation was obtained 22 d post-burst showing the afterglow had brightened at both 9 and 18 GHz. The resulting flux densities and 3σ upper limits (three times the rms) can be found in Table 3.

3 PROMPT EMISSION ANALYSIS

3.1 Joint spectral analysis

We performed a joint fit of the *Fermi*/GBM, *Swift*/BAT, and *SVOM*/GRM data to maximize the signal-to-noise ratio, allowing more robust constraints on spectral parameters. Spectra were extracted in the same time intervals as *Fermi*/GBM as defined in

Table 3. Radio flux density measurements of the radio afterglow of GRB 241105A. All errors are 1σ. The 3σ thresholds are three times the rms and correspond to the upper limit for all non-detections.

Time post-burst (d)	Frequency ν (GHz)	Flux density (μJy beam^{-1})	3σ threshold (μJy beam^{-1})
4.8	5.5	–	54
4.8	9.0	–	39
15.0	5.5	–	36
15.0	9.0	115 ± 43	33
17.1	18.0	343 ± 46	96
22.1	5.5	47 ± 45	114
22.1	9.0	220 ± 61	78
22.1	18.0	571 ± 154	180

Section 2.1.1. The fitting was performed in XSPEC v12.14.1 (Arnaud 1996). We fit the power-law, Comptonized, and Band function models and compare their goodness-of-fit statistics using Akaike's Information Criterion (Akaike 1974). A more complex model is preferred when $\Delta_{\rm AIC} \geq 4$, otherwise the simpler model is chosen. Free normalizations were included in the model fits to account for the relative effective areas between detectors on the different satellites. We found that the GRM detectors also required free normalizations relative to one another, as determined by $\Delta_{\rm AIC}$. We found that the inclusion of *SVOM*/GRM for the episode 2 and complete burst fits only added noise and resulted in a less constrained fit, so these epochs were fit with *Fermi*/GBM and *Swift*/BAT data only. The best-fitting models are presented in Table 4. Using these values, we computed the isotropic-equivalent energies and source-frame peak energies for both emission episodes and the whole burst, which are reported in Table 4.

3.2 Spectral lag

We computed the spectral lag, which refers to the delay in the arrival times of low-energy photons relative to high-energy photons. Long GRBs typically exhibit significant spectral lags, with delays of up to a few seconds in their light curves across different energy channels. In contrast, short GRBs generally show little or no spectral lag (Cheng et al. 1995; Yi et al. 2006). For *Swift*/BAT data, we estimated the lag between the 15–25 and 50–100 keV light curves using the cross-correlation function method (Bernardini et al. 2015). The lag is found to be $\tau_{\rm CC} = 376 \pm 11$ ms. Also, an anticorrelation between the bolometric peak luminosity and the spectral lag of GRBs has been identified by Norris (2002), and subsequently confirmed by Gehrels et al. (2006) and Ukwatta et al. (2010). Fig. 5 shows the position of GRB 241105Ain the lag–luminosity plane. The burst lies within the 2σ region of the correlation defined by long GRBs, as also seen previously for the short collapsar GRB 200826A (Rossi et al. 2022; Dimple et al. 2022b). For *Fermi*/GBM data, we computed the spectral lag between the 25–50 and 100–300 keV light curves.

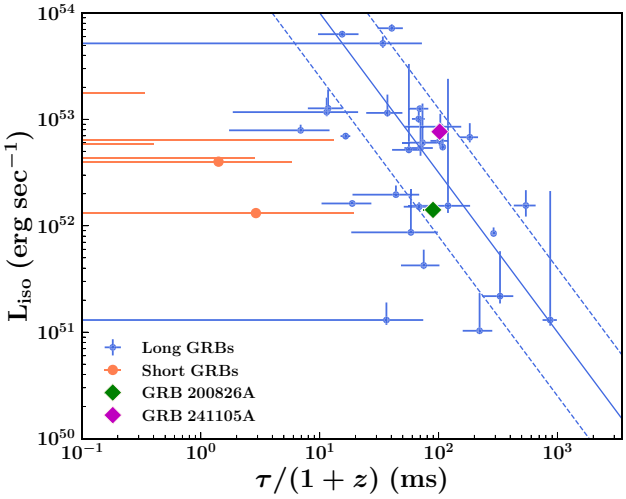

Figure 5. Lag–luminosity correlation of GRBs using data from Ukwatta et al. (2010). GRB 241105A follows the lag–luminosity trend typical of long GRBs, unlike short GRBs.

The lag is found to be $\tau_{\rm CC} = 130.8 \pm 230.8$ ms, and is therefore too poorly constrained to be informative.

3.3 Hardness ratio

We computed the hardness ratio (HR) as the fluence ratio between higher and lower energy bands, using data from both *Swift*/BAT and *Fermi*/GBM for both the emission episodes as mentioned in Section 2.1. Using *Swift*/BAT data, we calculated the HR between the 50–100 and 25–50 keV bands. For episode 1 (T_0–0.256 to T_0 + 1.28 s), the HR is measured to be 1.34 ± 0.17. For episode 2, the HR is 1.60 ± 0.25, and for the whole burst duration, it is 1.58 ± 0.20. We fitted a Bayesian Gaussian mixture model (BGMM) in the T_{90} versus HR distribution, using the *Swift*/BAT sample (Lien et al. 2016), to estimate the likelihood of the burst belonging to the short or long GRB classes. Fig. 6 shows the location of GRB 241105A in the HR–T_{90} plane relative to these EE GRBs. The background contours represent the probability density distribution of the two Gaussian components (dividing them into two classes, class 1 and class 2) derived from the fitted BGMM model. The probability of episode 1 belonging to class 1 (which is closer to short GRBs) is $P(\text{class 1}) = 0.886$, indicating a strong association with the short-hard GRB population. In contrast, episode 2 yields $P(\text{class 1}) = 0.030$, aligning more closely with the long-soft GRB class. The whole emission has $P(\text{class 1}) = 0.032$, which also aligns with a long burst.

We also performed an HR analysis using GBM data, calculating the fluence ratio between the 50–300 and 10–50 keV bands. The HR for episode 1 is 0.856 ± 0.211, while for the whole burst it decreases to 0.625 ± 0.034. The HR for episode 2 alone is 0.354 ± 0.328,

Table 4. Spectral fitting results for GRB 241105A in different time intervals. Uncertainties correspond to 1σ confidence intervals.

Emission region	Time range (s)	Model	Flux[a]	$E_{\rm p}$ (keV)	α	β	$E_{\rm iso}$[b]	χ^2/d.o.f.
Episode 1	−0.256 to 1.28	Band	12.4 ± 0.4	$312.0^{+168.2}_{-134.1}$	$1.15^{+0.12}_{-0.17}$	$2.08^{+0.29}_{-0.15}$	$3.20^{+0.10}_{-0.10}$	1.13
Episode 2	1.28 to 64.961	Cut-off PL	$1.12^{+0.05}_{-0.06}$	$3127.8^{+3015.7}_{-1750.3}$	$1.25^{+0.11}_{-0.12}$	–	$11.97^{+0.53}_{-0.64}$	1.79
Whole burst	−0.256 to 64.961	Cut-off PL	$1.43^{+0.05}_{-0.06}$	$2381.6^{+2014.0}_{-1291.2}$	$1.24^{+0.09}_{-0.11}$	–	$15.65^{+0.55}_{-0.66}$	1.78

Note. [a] Flux is given in units of 10^{-7} erg s^{-1} cm^{-2}. [b] Isotropic equivalent energy $E_{\rm iso}$ is in units of 10^{52} erg.

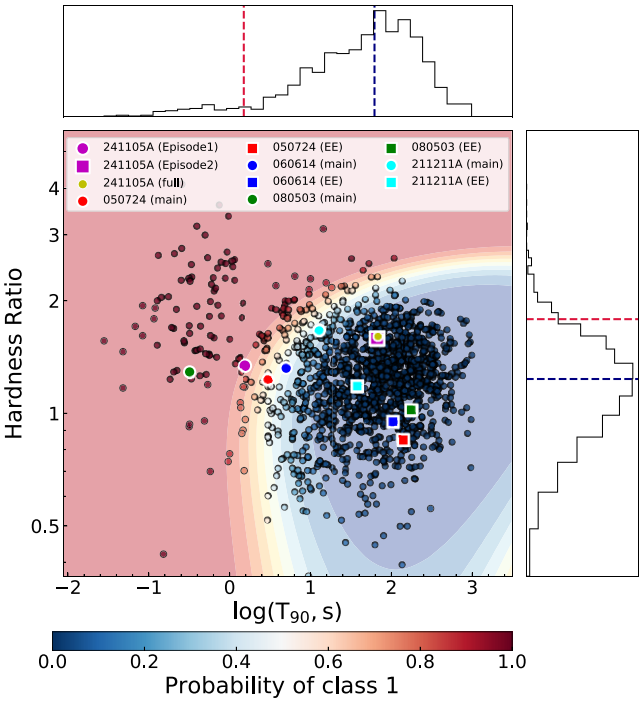

Figure 6. The positions of GRB 241105A (episodes 1 and 2) are shown in the log (T_{90})–HR plane, overlaid on the *Swift*/BAT GRB population alongside three well-known short GRBs with EE and long mergers with EE. The background contours represent the probability density of two components identified by the BGMM, corresponding to the short-hard and long-soft GRB classes, with the colour bar indicating the probability of belonging to the short class. Marginal histograms show the distributions of T_{90} and HR, with dashed lines marking the mean values for each class.

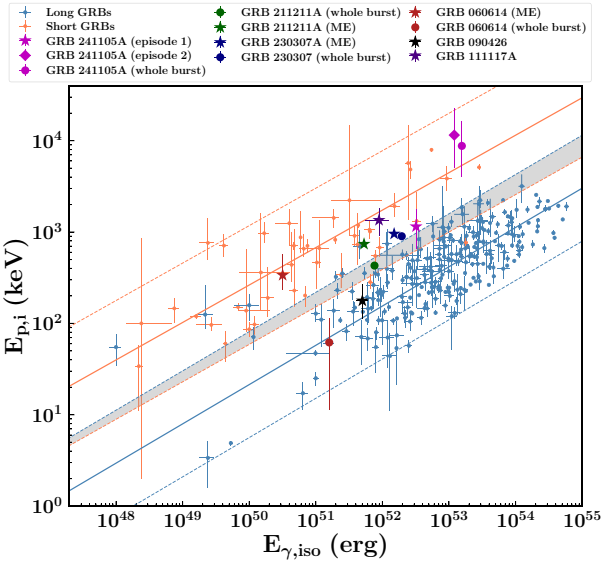

Figure 7. Location of GRB 241105A on the Amati plane ($E_{p,i}$ versus $E_{\gamma,\rm iso}$) along with short and long GRBs using the data set from Minaev & Pozanenko (2020).

although this measurement is affected by larger uncertainties due to lower photon statistics.

Further, we examined whether this burst aligns with classical EE GRBs, characterized by a hard initial spike followed by softer, prolonged emission (Norris & Bonnell 2006; Perley et al. 2009). We compared the HR of GRB 241105A with three well-studied short GRBs exhibiting EE: GRB 050724 (Barthelmy et al. 2005b), GRB 060614 (Gehrels et al. 2006), and GRB 080503 (Perley et al. 2009), as shown in Fig. 6. We also included the long merger GRB 211211A in our analysis, which also exhibits the characteristics of an EE burst. In typical EE events, the extended component is spectrally softer than the initial spike (e.g. Kaneko et al. 2015). However, in the case of GRB 241105A, we find that the second episode is spectrally harder than the first, in contrast to the canonical soft EE. While the temporal structure superficially resembles EE GRBs, the distinct spectral behaviour suggests that episode 2 may not represent a classical EE component.

3.4 Location on the Amati plane

Using the values derived in Section 3.1, we placed episodes 1, 2, and the whole burst in the Amati plane, alongside the short and long GRBs, using the data set from Minaev & Pozanenko (2020) as shown in Fig. 7. Episode 1 lies near the overlapping region of long and short GRBs. However, episode 2 and the whole burst are located within the region typically occupied by short GRBs. It is important to note that this comparison involves a heterogeneous data set compiled from multiple instruments and missions, each with differing sensitivities, calibrations, and analysis methodologies, which may introduce systematic uncertainties in the derived parameters. We also locate GRB 090426 and GRB 111117A, short GRBs at redshift $z > 2$. Interestingly, GRB 090 426 is located within the region typically occupied by long GRBs in the Amati plane. In addition, the main emissions (MEs) and whole emissions of GRB 060614, GRB 211211A, and GRB 230307A (compiled from Zhu et al. 2022; Peng, Chen & Mao 2024) are also included in our sample, which are long mergers with EE, as confirmed either by the detection of a kilonova or the exclusion of an SN.

3.5 ML insights

In addition to traditional classification methods, ML has become an indispensable tool in clustering GRBs, enabling the identification of underlying patterns and subpopulations within their complex data sets (Jespersen et al. 2020; Dimple et al. 2023, 2024b). To investigate the properties of GRB 241105A, we employed an ML pipeline that integrates principal component analysis (PCA; Hotelling 1933) with uniform manifold approximation and projection (UMAP; McInnes, Healy & Melville 2018). This analysis utilized prompt emission light curves from the *Fermi*/GBM catalogue across three energy bands – 8–50, 50–300, and 300–1000 keV – with a temporal resolution of 16 ms. We pre-processed the light curves by normalizing the fluence, aligning the start times, zero-padding to achieve uniform duration, and applying a discrete-time Fourier transform to preserve temporal delay signatures as detailed in Dimple et al. (2023, 2024b). We first used PCA to reduce the dimensionality of the data by transforming it into orthogonal principal components, retaining approximately 99 per cent of the total variance to capture salient features of the data while suppressing noise. Subsequently, UMAP is used to project the PCA-reduced data into a 2D embedding space, preserving both local and global structures through a topological similarity matrix. We optimized UMAP's performance using the hyperparameters `n_neighbors` = 25 and `min_dist` = 0.01, identified through iterative tuning.

Fig. 8 shows the connectivity map for *Fermi*/GBM bursts. In this map, GRBs lying close to each other suggest that they share

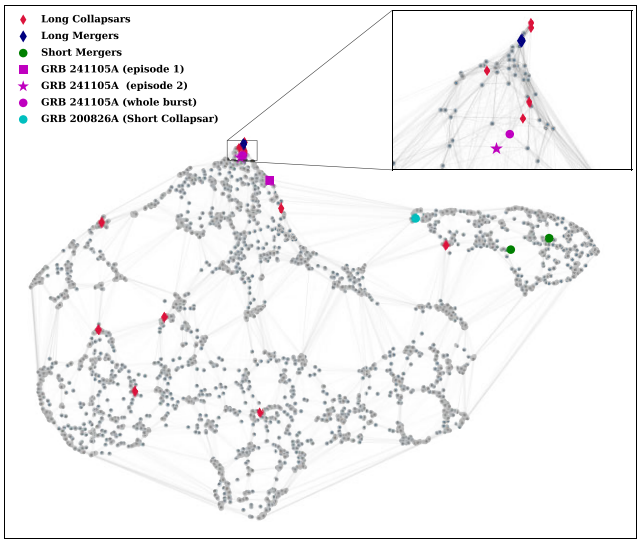

Figure 8. 2D embedding obtained using UMAP initialized by PCA obtained using *Fermi*/GBM light curves in different energy bands. The distances between points in the embedding give an idea of the similarity between the two events.

similar properties in the high-dimensional feature space. As the input comprises prompt emission light curves, such similarity may not necessarily reflect progenitor type, but could instead indicate similarities in central engine behaviour or radiation mechanisms. The proximity of GRB 241105Ain the ML embedding to both collapsars and long-duration mergers indicates similarities in their central engines (e.g. black hole accretion or magnetar spin-down) or emission mechanisms (e.g. prolonged jet activity or synchrotron radiation), rather than a common progenitor. This degeneracy necessitates multiwavelength data to confirm the progenitor. In addition, we located both episodes separately on the map; it is interesting to see that even episode 1 lies in the cluster surrounded by long GRBs. Both episodes and the whole burst lie far from short-duration mergers, indicating that if GRB 241105A is merger-driven, it resembles long-duration mergers rather than short-duration mergers.

3.6 Minimum variability time-scale

MVT, which traces the shortest resolvable time-scales in the light curve, provides constraints on the size and dynamics of the emitting region and the central engine (MacLachlan et al. 2013; Golkhou, Butler & Littlejohns 2015; Camisasca et al. 2023; Maccary et al. 2025). We estimated the MVT following the method of Golkhou et al. (2015), using both *Swift*/BAT and *Fermi*/GBM data following Golkhou et al. (2015). For the *Fermi*/GBM data in the 8–900 keV energy range, episode 1 exhibits an MVT $= 0.31 \pm 0.09$ s, while episode 2 shows a significantly longer MVT of 22.58 ± 4.07 s. These values are illustrated in Fig. 9, which shows the MVT distribution for the *Fermi*/GBM sample from Golkhou et al. (2015). The yellow and green lines mark the MVTs for both episodes, respectively, while the red and blue dashed lines indicate the mean MVT values for the short and long GRB populations. The MVT of the first episode falls between the characteristic mean values for short and long GRBs. In contrast, the second component aligns closely with the long GRB population, exhibiting longer variability time-scales. Similar trends are seen for *Swift*/BAT data in the 15–350 keV band, where we find that episode 1 has an MVT of 0.50 ± 0.17 s, while episode 2 exhibits

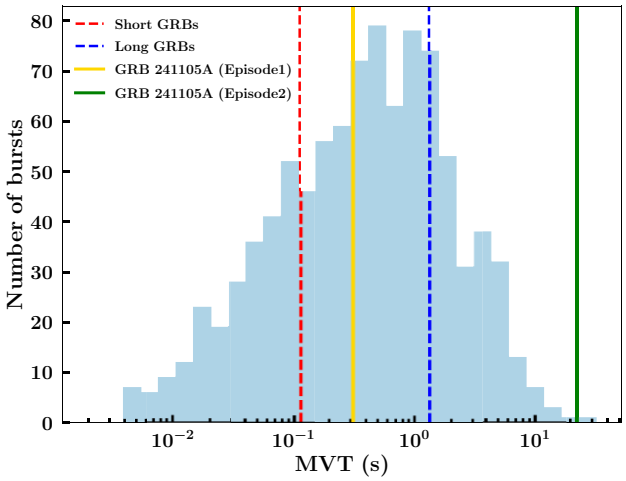

Figure 9. MVT histogram using *Fermi*/GBM sample from Golkhou et al. (2015). The yellow and green lines represent the MVT for both the emission episodes. The dotted lines show the mean value of MVT for short (red) and long (blue) GRB populations.

a significantly longer MVT of 27.37 ± 0.15 s. These results suggest a notable transition in the temporal properties of GRB 241105A between the two emission episodes.

4 AFTERGLOW MODELLING

4.1 Model description

We modelled the afterglow observations of GRB 241105A within the standard synchrotron framework (Sari, Piran & Narayan 1998), where a point deposition of energy ($E_{\rm K,iso}$) into a circumstellar medium with density, $\rho = AR^{-k}$ generates a relativistic forward shock that accelerates electrons into a power-law distribution, $N_\gamma \propto \gamma^{-p}$ above a minimum Lorentz factor, $\gamma > \gamma_{\rm min}$. We considered two standard possibilities for the radial density profile: a uniform density interstellar medium (ISM) model ($k = 0$, $A \equiv n_0 m_p$; Sari et al. 1998) and a wind-like model ($k = 2$, $A \equiv 5 \times 10^{11}\,{\rm g\,cm^{-1}}\,A_*$; Chevalier & Li 2000). The observed spectral shape of the resulting radiation is described by three break frequencies: the self-absorption frequency, $\nu_{\rm a}$; the characteristic injection frequency, $\nu_{\rm m}$; and the cooling frequency, $\nu_{\rm c}$; as well as the flux density normalization, $F_{\nu,{\rm m}}$ (Granot & Sari 2002). We utilized the weighting prescription described in Laskar et al. (2014) to compute smooth light curves during transitions between the different asymptotic regimes (Granot & Sari 2002).

We assumed that the afterglow jet is viewed on-axis, such that the above prescriptions (relevant for spherical outflows) apply. In addition, we utilized the formalism described in Rhoads (1999) to incorporate the jet break effect. We accounted for inverse Compton cooling and Klein–Nishina corrections using the prescription provided by McCarthy & Laskar (2024). We included Milky Way extinction of $A_{\rm V,MW} = 0.03$ mag in our model (Schlafly & Finkbeiner 2011), and assume a Small Megallanic Cloud-type extinction for the host galaxy appropriate for GRB hosts (Schady et al. 2007, 2012), with $A_{\rm V}$ as a free parameter (Pei 1992). At radio wavelengths, we computed[5] the effect of scintillation for visualization purposes,

[5]We did not fold in the expected modulation due to scintillation as an additional source of systematic uncertainty for this data set, as doing so

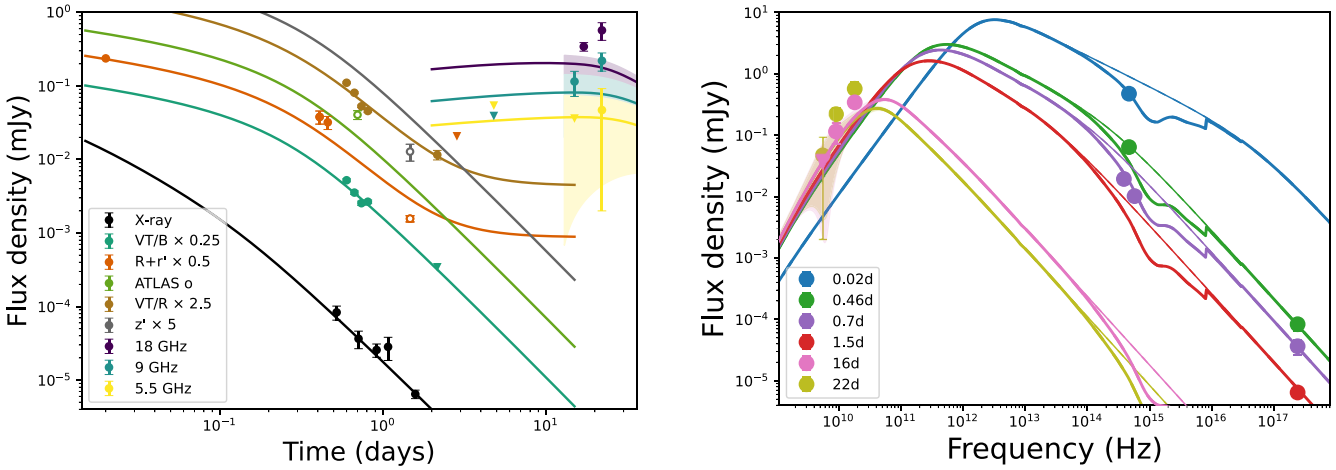

Figure 10. Light curves (left) and SEDs (right) for our best-fitting ISM model for the afterglow observations of GRB 241105A. Data points plotted in open symbols are not included in the analysis. Shaded bands indicate 1σ variability at each time expected from interstellar scintillation for reference. The flattening in the VT/*R*-band and $R + r'$-band light curves is due to a fixed host contribution of 1.8 μJy included in the modelling. Correlation contours for all physical parameters included in the fit, along with the derived parameters of $\theta_{\rm jet}$ and E_K, are presented in Fig. 11.

by computing the corresponding modulation index following the prescription of Goodman & Narayan (2006) as described in Laskar et al. (2014).

4.2 Data used in afterglow modelling

In addition to the UV/optical and radio observations reported here, we included X-ray data from *Swift*/XRT, which we converted from a count-rate to a flux density at 1 keV using the spectral model reported on the UKSSDC website (photon index, $\Gamma_X = 2.3$ and 0.3–10 keV unabsorbed counts-to-flux conversion factor, 3.9×10^{-11} erg cm^{-2} count^{-1}). We further included two epochs of follow-up observations taken with the Follow-up X-ray Telescope on board *Einstein Probe* at 0.92 and 1.58 d as reported by Zhou et al. (2024), which we also converted to flux density at 1 keV using the *Swift*/XRT photon index.

The wide filter bandpass of the *SVOM*/VT *R* and *B* bands (henceforth, VT/*R* band and VT/*B* band, respectively), along with the Lyman-α absorption in the spectrum (which lies within the *B* band) renders interband photometric comparison against other optical data challenging. To account for this, we derived a more accurate central wavelength for each filter given the observed spectrum. We fitted a continuum to the VLT spectrum using `contfit` in PYTHON and integrated the resultant model under the *SVOM*/VT filters, from which we computed effective wavelengths of 5218 and 7750 Å for the VT/*B* and *R* bands, respectively. We note that the latter is actually closer to i' band. In addition, we found that the integrated flux within each band is lower (and therefore needs to be increased) relative to the values of the continuum at the effective wavelength by 19 per cent in the VT/*B* band and 9 per cent in VT/*R* band. The flux suppression is higher in VT/*B* band due to Lyα absorption. Under the assumption that the spectral shape does not change significantly over the course of the *SVOM*/VT observations, we applied these corrections uniformly to the VT data in subsequent discussion in this section.

The NTT r' photometry at 1.47 d is a factor of 2.5 fainter than the expected flux density of ≈ 8 μJy expected from interpolating between the VT/*R* band points at ≈ 0.8 and ≈ 2.2 d. Additionally, the NTT z'–r' spectral index[6] of $\beta = 0.5 \pm 0.7$ is positive at this time, in strong contrast to the optical spectral index between the *SVOM*/VT *B* and *R* bands, which is $\beta_{R-B} = -2.08 \pm 0.16$ (even after the previously described correction, which increases the *B*-band flux more than that of the *R* band). Similarly, the ATLAS *o*-band observation at 0.7 d, nominally in between the VT/*B* and *R* bands in centre wavelength and obtained after the *SVOM* observations at 0.67 d, is nevertheless brighter than both, and cannot be easily explained. We therefore did not include the NTT or ATLAS photometry in our analysis and instead plotted these data points on subsequent figures as open symbols.

4.3 Preliminary modelling considerations

4.3.1 Optical and X-rays: Jet break, circumstellar density profile, host contribution, and relative locations of $\nu_{\rm m}$ and $\nu_{\rm c}$

We further investigated the light curves (Fig. 10, left panel) and spectral energy distributions (SEDs; Fig. 10, right panel) of the afterglow to inform our modelling. The X-ray light curve comprising three *Swift*/XRT points and two *Einstein Probe*/FXT points can be fitted with a single power law with a steep decay, $\alpha_{\rm X} = -2.3 \pm 0.2$ from 0.5–1.6 d. The optical light curve declines equally steeply during this period, with $\alpha'_r = -1.9 \pm 0.3$ from the BOOTES-7 data point at 0.41 d and the Gemini-South observation at 1.4 d. The *SVOM* optical light curves start at 0.6 d and are consistent with this steep decay, with $\alpha_{\rm VT-B} = -2.5 \pm 0.6$ and $\alpha_{\rm VT-R,1} = -3.0 \pm 0.6$. In the standard synchrotron framework, the steepest decline possible is in the regime $\nu_{\rm m} < \nu < \nu_{\rm c}$, with $\alpha = (1 - 3p)/4$ in the wind model. If the X-ray and optical bands are in this regime, then the X-ray decline rate would imply $p = 3.4 \pm 0.3$ and require a spectral index of $\beta = (1 - p)/2 = -1.2 \pm 0.1$. The observed spectral index between the VT/*R* band and the X-rays at ≈ 0.67 d is $\beta_{R-X} = -1.05 \pm 0.04$, which is consistent with the requirement.

significantly downweights the radio data, which is a specific concern for this rather small data set ($\sim$ 27 data points).

[6]We use the convention, $F_\nu \propto t^\alpha \nu^\beta$ throughout.

Although we are constrained in our modelling to $p < 3$ by our KN correction framework, which does not allow us to consider values of $p > 3$, we are able to find a model that matches the rough features of the light curves with $p \approx 3$; however, this model underpredicts the radio observations by factors of 5–10, and we do not discuss this case further. Instead, a more natural explanation is afforded by considering the steep decline to be associated with post-jet break evolution. In the remainder of this discussion, we focused on that scenario, which then indicates $t_{\rm jet} \lesssim 0.5$ d and $p \sim 2.3$.

Since the light-curve evolution is the same in both ISM and wind cases after the jet break, and very little data exist prior to 0.5 d (Fig. 10, left panel), it is not possible to determine the nature of the pre-explosion environment in this case. In the remainder of this section, we focused on the ISM case (which ends up providing a slightly lower reduced χ^2, as we discuss in Section 4.4), and present the wind model in Appendix A.

The temporal decline between the last two VT/*R*-band points at 0.81 and 2.16 d (Fig. 10, left panel) of $\alpha_{\rm VT-R,2} = -1.40 \pm 0.16$ is much shallower than $\alpha_{\rm VT-R,1} = -3.0 \pm 0.6$, consistent with the detection of the host galaxy in our *JWST* imaging (Section 2.3). In our subsequent analysis, we assumed a fixed[7] (and equal) host contribution in the r' and VT/*R* bands corresponding to a flux density of 1.8 μJy of the host measured in a 1 arcsec aperture within the closest *JWST* filter available (*F070W*; Table 2).

The temporal decay of $\alpha = -0.64 \pm 0.06$ between the GOTO *L*-band observation at 0.02 d and the VLT r'-band observation at 0.46 d is shallower than the slowest afterglow decay rate possible, which is $\alpha = (3 - 3p)/4 = -0.98 \pm 0.15$ in the $\nu_{\rm m} < \nu < \nu_{\rm c}$ regime. Instead, the fast-cooling model $\nu_{\rm c} < \nu < \nu_{\rm m}$ allows for the additional possibility of $\alpha = -2/3$ in the $\nu_{\rm a} < \nu < \nu_{\rm c}$ regime (wind case) and $\alpha = -1/4$ in the $\nu_{\rm c} < \nu < \nu_{\rm m}$ regime (wind or ISM case). We found that both are plausible; the first matches the observed decay closely, while the latter can still be accommodated with moving the jet break earlier. In either case, a fast cooling segment in the early light curves ($\lesssim 0.5$ days) is required, indicative of either a high magnetic field or a high-density environment, both of which can result in a lower cooling frequency. We return to this point in Section 4.3.2.

The spectral index between the VT/*R* and VT/*B* bands, $\beta_{\rm R-B} = -2.08 \pm 0.16$, is much steeper than the spectral index from either the VT/*R* band or the VT/*B* band to the X-rays, which are $\beta_{R-X} = -1.05 \pm 0.04$ and $\beta_{B-X} = -0.99 \pm 0.05$, respectively, indicating that extinction is present[8] (Fig. 10, right panel). The observed spectral index of $\beta \approx -1$ between the optical and X-rays is marginally shallower than the spectral index expected in the regime $\nu_{\rm m}, \nu_{\rm c} < \nu$ of $\beta = -p/2 = -1.15 \pm 0.10$, which may arise from either the aforementioned extinction or from a spectral break proximate to the optical wavelengths. Since the afterglow is expected to be in fast cooling, this is suggestive of the presence of $\nu_{\rm c}$ close to the optical bands. We return to this point in Section 4.4.

[7]While it is possible to keep this parameter free, we found that doing so results in best-fitting values differing by a factor of ≈ 3 between the two nearly identical bands, commensurate with the limited late-time ($\gtrsim 1$ d) photometric information available. In this situation, fixing this parameter to a reasonable value yields better model convergence.

[8]The X-ray spectral index from *Swift*/XRT, $\beta_{\rm X} = -1.3^{+0.8}_{-0.7}$ is consistent with the optical-to-X-ray spectral index, but is otherwise not constraining due to the large uncertainty.

4.3.2 Radio: synchrotron self-absorption

A power-law fit to the radio detections at ≈ 22 d yields a spectral index of $\beta_{\rm radio,22} = 1.7 \pm 0.4$, which is consistent with the spectral index between the ATCA *X* band (9.0 GHz) and *Ku*/15mm band (18 GHz) at 15–17 d $\beta_{\rm XU} = 2.4 \pm 1.0$ as well as with the 5 GHz non-detection in this earlier epoch, together indicating a strongly self-absorbed synchrotron spectrum, $\nu_{\rm a} \gtrsim 18$ GHz until ≈ 22 d, indicative of a high-density pre-explosion environment. This is consistent with the low cooling frequency inferred from the early ($\lesssim 0.5$ d) optical light curve, as discussed in Section 4.3.

In the framework where the radio emission arises from the afterglow forward shock and in the scenario that the jet break ($t_{\rm jet} \lesssim 0.5$ d) has already occurred at by the time the radio observations commence, the radio light curves are expected to be constant in this regime; instead, the light curves appear to rise both at 18 GHz ($\alpha_{\rm 18\,GHz} = 2.0 \pm 1.3$) and at 9 GHz ($\alpha_{\rm 9\,GHz} = 1.7 \pm 1.3$; and also at 5.5 GHz, although the rise rate in that band is much harder to measure, since the first two epochs yielded non-detections and the sole detection in the third epoch has very large uncertainties). This behaviour is unexpected in the standard framework (although, see also van Eerten et al. 2011). One possibility is that this may be due to scintillation; however, detailed analysis of this possibility requires additional radio observations. We nevertheless included the radio observations in our modelling and discuss deviations from the best-fitting model further in Section 4.4.

4.4 Markov Chain Monte Carlo Analysis

We explored the multidimensional likelihood space for the parameters of the afterglow model using a Markov Chain Monte Carlo (MCMC) with EMCEE. Further details of the modelling procedure, including the likelihood function employed, are described elsewhere (Laskar et al. 2013, 2014, 2016). To account for flux calibration offsets between observations across telescopes, we included a systematic uncertainty of 10 per cent added in quadrature to all measurements. We employed uniform priors on p and the extinction, A_V and Jeffreys (1946) priors for the remaining parameters ($\epsilon_{\rm e}$, $\epsilon_{\rm B}$, $E_{\rm K,iso,52}$, n_0, A_*, and $t_{\rm jet}$). We run 512 chains for 2000 iterations (testing for convergence by tracking the mean likelihood with iteration) and discard the initial 50 steps as burn-in.

As discussed above, we focused on the ISM model here and present the wind model in Appendix A. Our best-fitting ISM model has $p = 2.24, \epsilon_{\rm e} = 0.49, \epsilon_{\rm B} = 0.43, n_0 = 1.9 \times 10^2, E_{\rm K,iso} = 4.8 \times 10^{52}$ erg, $t_{\rm jet} = 0.13$ d, and $A_V = 0.19$ mag. For these parameters, $\nu_{\rm m} \approx 4.1 \times 10^{15}$ Hz at ≈ 0.1 d. This break passes through the optical bands between 0.1–0.4 d, consistent with the expectations in Section 4.3. The afterglow is in fast cooling with $\nu_{\rm c} < \nu_{\rm m}$. In this regime, the self-absorption break splits into two ($\nu_{\rm ac}$ and $\nu_{\rm sa}$), and for these parameters the spectral peak is at $\nu_{\rm sa} \approx 7.6 \times 10^{11}$ Hz with a peak flux density of ≈ 16 mJy. The cooling break, $\nu_{\rm c} \approx 3 \times 10^{10}$ Hz at this time and is unobservable, while $\nu_{\rm ac} \approx 1.1 \times 10^9$ Hz only crosses above 5.5 GHz at ≈ 7.5 d and is, therefore, weakly constrained. In this spectral regime,[9] the decline rate in the optical bands is $\alpha = -1/4$; this is steepened in the model light curves by the jet break, and the optical light curves further steepen subsequently when $\nu_{\rm m}$ passes through the observing band. We plot light curves and SEDs from the radio to X-rays of the best-fitting model in Fig. 10 and provide corner

[9]We note that in this regime where $\nu_{\rm sa}, \nu_{\rm c} < \nu < \nu_{\rm m}$ corresponding to the $F_\nu \propto \nu^{-1/2}$ spectral power-law segment, the optical light curves are insensitive to the density profile.

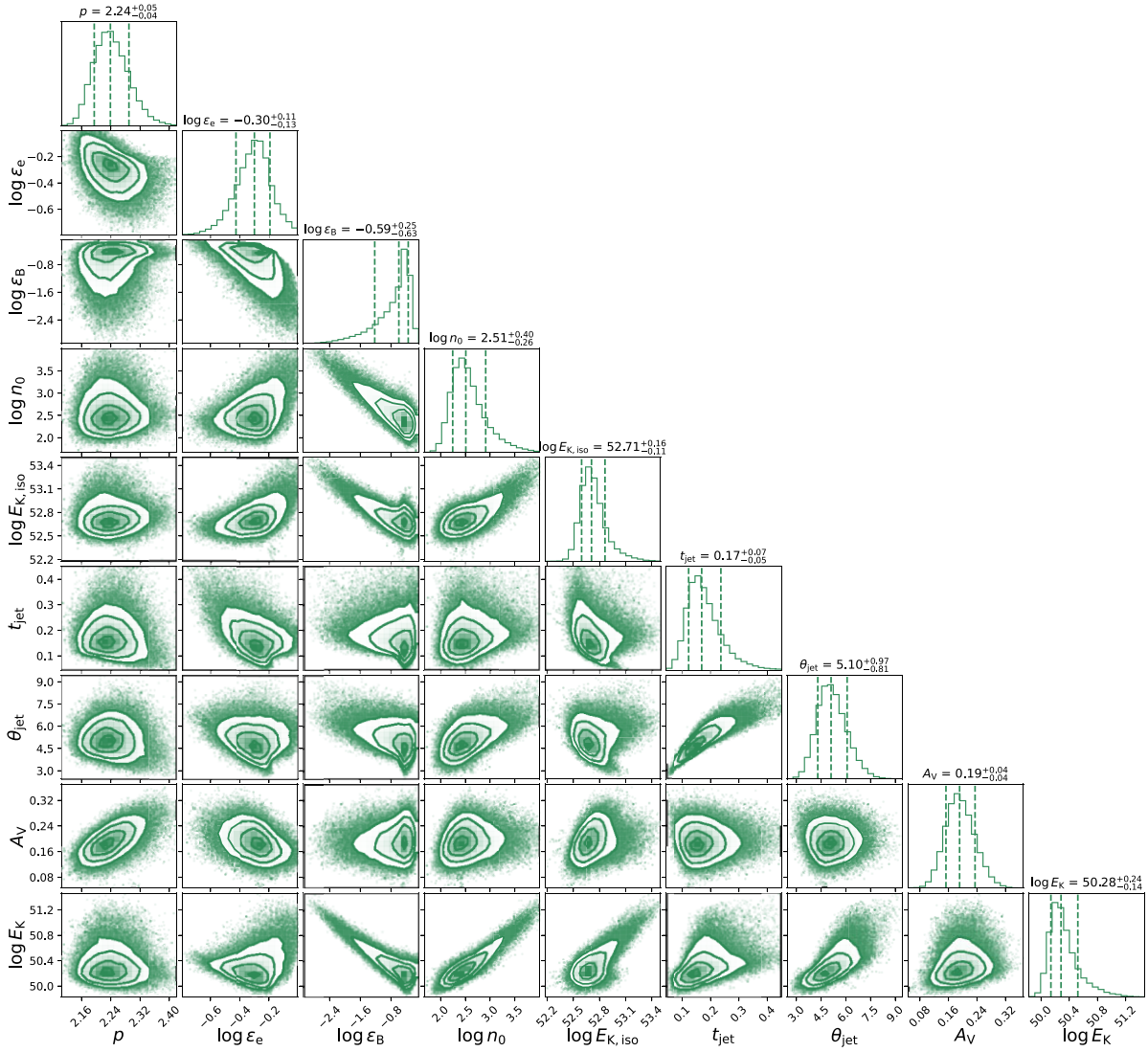

Figure 11. Correlations and marginalized posterior density for all free parameters in the afterglow model. $E_{K,iso}$ and E_K are in units of erg, t_{jet} in days, θ_{jet} in degrees, and A_V in magnitudes. The contours enclose 39.3 per cent, 86.4 per cent, and 98.9 per cent of the probability mass in each correlation plot (corresponding to 1σ, 2σ, and 3σ regions for 2D Gaussian distributions, respectively. The dashed lines indicate the 15.9 per cent, 50 per cent, and 84.1 per cent quantiles, corresponding to the median and $\pm 1\sigma$ for 1D Gaussian distributions.

plots of the correlations and marginalized posterior density for all fitted parameters (and the derived parameters, θ_{jet} and E_K) from our MCMC analysis in Fig. 11. We list our derived parameters in Table 5.

The contour plots reveal correlations between the physical parameters. Upon investigation, we associate these degeneracies with a range of allowed values for the Compton Y-parameter that nevertheless result in similar light curves and SEDs in the absence of a clear identification of the cooling break (the latter being hidden below ν_{sa} for all parameter ranges spanned by this model). Following the framework of Laskar et al. (2014), we quantify these degeneracies by explicitly asking which segments of the SEDs are constrained by the data. From Fig. 10, we identify these to be the flux on power-law segments C, F, and H (Granot & Sari 2002), $F_C \equiv F_{\nu_{ac}<\nu<\nu_{sa}}$, $F_F \equiv F_{\nu_{sa}<\nu<\nu_m}$, and $F_H \equiv F_{\nu<\nu_m}$, which are constrained by the radio, optical, and X-ray observations, respectively. Solving for the physical parameters in terms of these three fluxes and the (unobserved) cooling frequency, while accounting for the expected effects of IC cooling as described in Granot & Sari (2002), we expect $\epsilon_e \propto \nu_c^{-1/4}$, $\epsilon_B \propto \nu_c^{7/4}$, $n_0 \propto \nu_c^{-5/4}$, and $E_{K,iso} \propto \nu_c^{-3/4}$. The resulting expected correlations between the physical parameters due to the unknown value of ν_c are then $E_{K,iso} \propto n_0^{3/5} \propto \epsilon_B^{-3/7} \propto \epsilon_e^3$, $n_0 \propto \epsilon_e^5 \propto \epsilon_B^{-5/7}$, and $\epsilon_B \propto \epsilon_e^{-7}$, all of which are fully consistent with the sense and roughly consistent with the slopes of the corresponding observed correlations. Since ν_c is unobservable in this model,[10] few observational constraints could help resolve this particular degeneracy.

[10]We note that in the standard framework ignoring IC cooling, ν_c can be inferred using a combination of ν_{sa}, ν_{ac}, and ν_m; however, the addition of Compton Y as an additional parameter results in the specific degeneracies described here.

Table 5. Afterglow model parameters.

Parameter	ISM		Wind[a]	
	Best fit	MCMC	Best fit	MCMC
p	2.24	$2.24^{+0.05}_{-0.04}$	2.21	$2.21^{+0.05}_{-0.04}$
$\log \epsilon_e$	−0.31	$-0.30^{+0.11}_{-0.13}$	−0.31	$-0.23^{+0.14}_{-0.17}$
$\log \epsilon_B$	−0.37	$-0.59^{+0.25}_{-0.63}$	−0.81	$-1.21^{+0.67}_{-1.01}$
$\log n_0$	2.27	$2.51^{+0.40}_{-0.26}$	...	...
$\log A_*$	...	...	0.40	$0.63^{+0.55}_{-0.32}$
$\log(E_{K,iso}/erg)$	52.7	$52.71^{+0.16}_{-0.11}$	52.7	$52.75^{+0.35}_{-0.19}$
A_V/mag	0.19	0.19 ± 0.04	0.20	0.19 ± 0.04
t_{jet}/days	0.13	$0.17^{+0.07}_{-0.05}$	0.17	$0.20^{+0.08}_{-0.05}$
θ_{jet}/deg	4.31	$5.10^{+0.97}_{-0.81}$	4.62	$5.23^{+1.11}_{-0.85}$
$\log(E_K/erg)$	50.1	$50.28^{+0.24}_{-0.14}$	50.2	$50.35^{+0.47}_{-0.25}$
$\log(\nu_{ac}/Hz)$[b]	9.1	...	9.2	...
$\log(\nu_{sa}/Hz)$	11.9	...	12.0	...
$\log(\nu_c/Hz)$[b]	10.5	...	9.0	...
$\log(\nu_m/Hz)$	15.6	...	15.4	...
$F_{\nu,sa}$/mJy	15.9	...	13.6	...

Note. [a] The wind model is discussed further in Appendix A. [b] This break frequency is not directly constrained by the data. All break frequencies and fluxes are provided at 0.1 d.

Table 6. List of transitions and corresponding column densities of low- and high-ionization absorption lines identified in the GRB 241105A VLT/FORS2 spectrum using the Voigt fit procedure. All listed transitions are observed at the common redshift $z = 2.681$. Column density measurements are derived assuming a Doppler parameter $b = 118 \pm 20\,km\,s^{-1}$ from the simultaneous fit of low-ionization transitions with a single component. High-ionization transitions exhibit a blueward shift of $\sim -150\,km\,s^{-1}$ and a larger Doppler parameter $b = 143 \pm 20\,km\,s^{-1}$. Saturated transitions are reported as 3σ lower limits to maintain conservatism given resolution and hidden saturation effects.

Transitions (Å)	$\log(N/cm^{-2})$
S II λ1253, λ1255, λ1259	> 15.0
Si II λ1260, λ1304, λ1527, λ1808	16.1 ± 0.2
Si II* λ1264, λ1265, λ1533	14.0 ± 0.2
O I λ1302	> 16.5
C II λ1334	> 16.0
C II* λ1335	> 14.5
Fe II λ1608, λ2344, λ2374, λ2382, λ2587, λ2600	15.1 ± 0.2
Al II λ1670	> 14.2
N V λ1238, λ1242	> 14.4
Si IV λ1393, λ1402	> 15.1
C IV λ1548, λ1550	> 14.4
Al III λ1854, λ1862	> 13.9

5 HOST CHARACTERISTICS

5.1 Kinematics of the host environment

As described in Section 2, the VLT/FORS2 spectrum of the afterglow of GRB 241105A shows a strong Lyα absorption trough and numerous metal absorption lines at a common redshift of $z = 2.681$, which we adopt as the systemic redshift of the host galaxy. We estimated the neutral hydrogen column density (N_{HI}) along the line of sight to GRB 241105A from the broad Lyα absorption feature observed at the host redshift. The absorption profile is modelled using `VoigtFit` (Krogager 2018), incorporating the spectral resolution of the data. The redshift (z) and Doppler parameter (b) were fixed to the values derived from metal line fitting (see below), leaving N_{HI} as the only free parameter. The best-fitting model yields $\log(N_{HI}/cm^{-2}) = 21.15 \pm 0.10$, consistent with values commonly observed in long GRB hosts at $z \gtrsim 2$ (Jakobsson et al. 2006; Fynbo et al. 2009; Selsing et al. 2019; Heintz et al. 2023).

We fitted the identified metal absorption lines with the ASTROCOOK software (Cupani et al. 2020), a PYTHON code environment to analyse spectra modelled with Voigt profiles, depending on the system redshift z, its column density N, and its Doppler broadening b. The Voigt profile fitting of each identified transition is shown in Fig. 12 and the corresponding column densities are reported in Table 6. We infer a high Doppler parameter (i.e. $b = 118 \pm 20\,km\,s^{-1}$ for low-ionization absorption lines) given the resolution of the spectrum, hence we are not able to really dissect the ISM into several gas cloud components. Furthermore, several absorption lines are saturated and we decide to provide 3σ column density lower limits. There are a few exceptions such as Si II, Si II*, and Fe II, given the flux residuals of some transitions belonging to the same multiplet which allowed us to provide a column density measurement.

To cross-validate the Voigt profile fitting, we also performed a curve-of-growth (CoG) analysis using a subset of unblended lines of low-ionization electronic transitions. The Doppler parameter obtained by constraining the CoG with several equivalent width (EW) measurements (by using a combination of the lines with different oscillator strengths) is $b = 112.3 \pm 35.8\,km\,s^{-1}$, consistent with the Voigt results. A potential overestimate in the column density of C II is noted due to unresolved blending with C II*. Further details of the CoG fitting procedure and results are provided in Appendix B.

5.2 Host SED fitting

We fit the available *JWST* photometry with PROSPECTOR (Johnson et al. 2021), with a delay τ star formation history (SFH) and BPASS for the spectral synthesis (Eldridge et al. 2017; Stanway & Eldridge 2018). We let the stellar mass, visual attenuation, SFH e-folding time, and burst age vary freely within flat priors, and explored the parameter space using MCMC sampling with EMCEE (Foreman-Mackey et al. 2013). Metallicity is treated with a top-hat prior, with lower and upper bounds of $\log_{10}(Z/Z_\odot) = -1.3$ and 0.3, respectively. The lower bound is constrained by [S/H], as measured in the afterglow spectrum. The predicted SED of the host galaxy, along with the measured photometry, is shown in the left panel of Fig. 13. The properties derived from the fit shown in Table 7 (see also Fig. 14) indicate the host galaxy is rather massive, star-forming, and with low metallicity.

To investigate whether there are significant variations across the host, we aligned the six *JWST* images, degrading the short-wavelength filters to the same pixel scale as the long wavelengths, and smoothing each with a Gaussian filter to match the FWHM of the *F070W* image. We then selected pixels with a flux level more than 5σ above the background in all six filters, in a 10×10 pixel region around the GRB location, and plotted their SEDs in the right panel of Fig. 13. Although the pixel SEDs show deviations on a filter to filter level, the overall SED shape is similar across the host. We therefore deem the host-integrated properties (namely extinction, age, and metallicity) to be representative of the transient location, although we caution that metallicities from SED fitting do suffer from systematics (Leja et al. 2019; Johnson et al. 2021).

5.3 GRB offset and host morphology

We determined the position of the afterglow in the *JWST* reference frame by identifying sources in common between the stacked FORS2

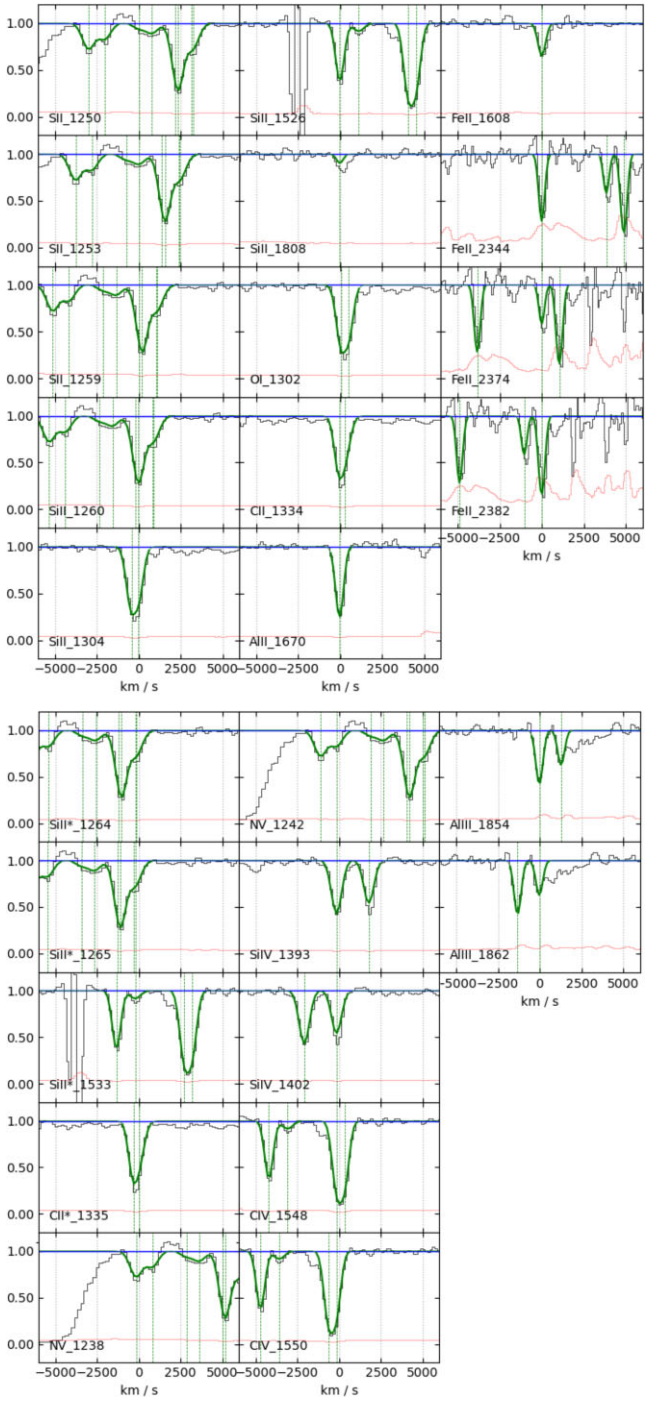

Figure 12. VLT/FORS2 optical afterglow spectrum of GRB 241105A at redshift $z = 2.681$. Top panel: low-ionization absorption lines of the GRB host galaxy system. Here and in the bottom panel data are in black, the fit is in green, the error spectrum is in red, the continuum in blue and the vertical green dashed lines indicate the centre of the components. Bottom panel: fine structure lines and high-ionization absorption lines.

g-band detection images, and the *F070W JWST* image. Using DAOStarFinder routines in PHOTUTILS module of PYTHON (Bradley et al. 2024), we found five good cross-match objects which are compact and symmetrical. The field is relatively sparse with few suitable cross-match objects, others were available but rejected due to saturation or diffuse/EE (i.e. galaxies) for which the centroid is less certain. We fixed the transformation between the two known pixel scales and allow for x–y shifts and rotation, to find a mapping from the FORS2 reference frame to that of the *JWST* image which minimizes the root mean square (rms) of the positional offsets post-transformation. The rms of the final transformation is 36 mas. The positional uncertainty of the afterglow centroid in the FORS2 image (given by the FWHM/(2.35×SNR)) is 16 mas, for a total positional uncertainty of the afterglow in the *JWST* frame of 39 mas. The burst location is shown in Fig. 4.

We also measured the morphological properties of the host galaxy with STATMORPH (Rodriguez-Gomez et al. 2019). A Sérsic fit (shown in Fig. 15 yields a half-light radius $r_{50} = 170$ mas, if we take the galaxy (which is composed of two prominent clumps) as one object. At $z = 2.681$ this corresponds to a physical size of 1.4 kpc. Using the x, y centroid of the galaxy from the STATMORPH Sérsic fit and the refined afterglow position, we found a projected host offset of 23^{+37}_{-23} mas, or $0.18^{+0.29}_{-0.18}$ kpc. The uncertainties are at the 1σ level and are calculated assuming a Rice distribution. The corresponding host-normalized offset is $r_{\rm norm} = 0.13^{+0.21}_{-0.13}$. Such a low projected offset is routinely observed for collapsar GRBs (albeit at the low end of the distribution), and extremely rare for compact object merger progenitors (e.g. Fong et al. 2022). Furthermore, the concentration and asymmetry values for the host galaxy ($C = 2.97$ and $A = 0.27$, respectively) lie in the spiral/irregular/merger region in C–A parameter space. This is consistent with its star-forming nature, and with the population of collapsar host galaxies (Conselice et al. 2005; Schneider et al. 2022).

6 DISCUSSIONS

6.1 An ambiguous 'short + EE' burst

GRB 241105A, with a initial short spike followed by prolonged, weaker emission, places it firmly within the so-called short + EE GRB population. While this two-component profile is a defining characteristic of these events, GRB 241105A exhibits a crucial difference that sets it apart from the classical examples of merger-driven EE GRBs like GRB 060614, GRB 211211A, and GRB 230307A. The EE in the case of GRB 241105A is not as spectrally soft as typically observed in these well-studied events. Similar behaviour has been noted in other nominally short GRBs at higher redshifts (Dichiara et al. 2021), where EE is seen in the higher energy bands for short GRBs with $z > 1$, challenging the conventional definition of EE GRBs.

6.2 A bright afterglow

We compared the X-ray (0.3–10 keV), optical (R band), and radio light curves of GRB 241105A with the short GRB population. The leftmost panel of Fig. 16 presents the X-ray light curves (in the 0.3–10 keV band) for a sample of short GRBs, shown in grey, with GRB241105A overplotted in magenta. The flux light curves were taken from the *Swift* XRT repository[11] and converted to rest-frame luminosities using standard cosmological parameters. As is evident from the figure, GRB241105A exhibits significantly higher X-ray luminosity than the majority of short GRBs at comparable epochs.

In the central panel of Fig. 16, we show the rest-frame R-band light curves of short GRB afterglows, compiled from the data

[11] https://www.swift.ac.uk/xrt_curves/

Table 7. Host-galaxy properties of GRB 241105A. The uncertainties correspond to 1σ confidence intervals.

Parameter	Value
$\log(M_*/M_\odot)$	$10.16^{+0.04}_{-0.02}$
SFR [$M_\odot$ yr^{-1}]	135^{+456}_{-102}
t_{age} (Gyr)	$0.37^{+0.20}_{-0.14}$
$\log(Z/Z_\odot)$	$-1.03^{+0.13}_{-0.12}$
A_V (mag)	$0.18^{+0.25}_{-0.14}$
Offset (kpc)	$0.18^{+0.29}_{-0.18}$

sets of Fong et al. (2015) and Rastinejad et al. (2021), plotted in grey. GRB241105A is again shown in magenta. All magnitudes are corrected for Galactic extinction and converted to flux densities. Among the entire short GRB sample, GRB241105A stands out as the brightest known optical afterglow.

Only 18 confirmed short (merger driven) GRBs have been detected in the radio band (Berger et al. 2005; Soderberg et al. 2006; Fong et al. 2014, 2015, 2021; Lamb et al. 2019; Troja et al. 2019; Laskar et al. 2022; Chastain et al. 2024; Levan et al. 2024; Schroeder et al. 2024, 2025a; Anderson et al. 2024a; Schroeder, Fong & Laskar 2025b), representing 13 per cent of the population (Schroeder et al. 2025a). Note that we include the long-duration merger GRB 230307A (Levan et al. 2024) in this sample but not GW170817/GRB 170817A (Abbott et al. 2017). Two-thirds of this radio-detected sample was detected within $1-2$ d post-burst, most of which faded below detectability within 4–9 d (Anderson et al. 2024a), indicating short GRBs usually have short-lived radio afterglows. Meanwhile, GRB 241105A was undetected by ATCA at ~ 5 d, but then the rising radio afterglow was detected at 15 d (see Table 3). GRB 210726A is the other example of a short GRB that was undetected in the radio band until > 10 d post-burst, at which point it underwent a radio flare between $11-62$ d that was likely caused by energy injection or a reverse shock from a shell collision (Schroeder et al. 2024). The evolution of the radio light curve of GRB 241105A is quite different from that of the radio-detected short GRB population, which in nearly all cases are declining by ~ 6 d in the rest frame when GRB 241105A still appears to be brightening (see the left panel of Fig. 16).

GRB 241105A is also more radio luminous than the radio-detected short GRB population. As shown in the rightmost panel of Fig. 16, the majority of these short GRBs have a radio luminosity $\lesssim 10^{30}$ erg s^{-1} Hz^{-1}, which is fainter than long GRBs (radio luminosities usually between $\sim 10^{30}-10^{32}$ erg s^{-1} Hz^{-1} up to ~ 100 d post-burst; Chandra & Frail 2012; Anderson et al. 2018). Only GRB 241105A and GRB 210726A are more luminous than the average radio luminosity of long GRBs of 1.1×10^{31} erg s^{-1} Hz^{-1}, with GRB 241105A being the only one brighter than a canonical long GRB mean luminosity of $\sim 2\times10^{31}$ erg s^{-1} Hz^{-1} between 3–6 d in the rest frame (Chandra & Frail 2012). As a result, the radio luminosity and evolution of GRB 241105A is more consistent with the long GRB radio-detected population.

The prompt efficiency ($\eta_\gamma \approx 75$ per cent; see Tables 5 and 8) of the whole burst is high but nevertheless consistent with the median η_γ for both long- and short-duration GRBs (Zhang et al. 2007; Fong et al. 2015; Laskar et al. 2015). On the other hand, the isotropic-equivalent kinetic energy derived from multiwavelength afterglow modelling is more typical of long-duration collapsar GRBs than of short, merger-driven bursts (Fong et al. 2015). Similarly, the circumburst density is orders of magnitude higher than the densities commonly inferred for compact-object merger environments (Fong et al. 2015). Such high circumburst densities are extremely rare for merger-driven GRBs, but are common in the actively star-forming, gas-rich environments of collapsar events (Schulze et al. 2011).

6.3 A star-forming galaxy

The host galaxy of GRB 241105A is moderately massive, actively star-forming, and metal-poor. We compared the host properties of GRB 241105A with the short GRB population using data from

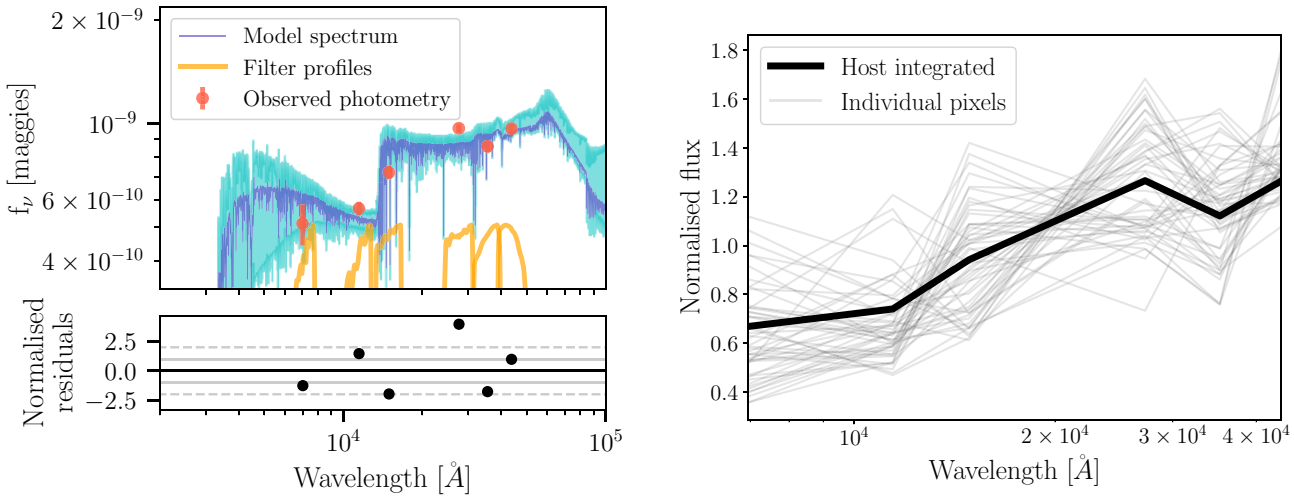

Figure 13. Left: results of the PROSPECTOR fit to the host photometry. Upper panel: best-fitting SED in blue, the shaded light blue region represents the 2σ uncertainty of the predicted SED at each wavelength. All wavelengths are in the observer frame. The orange markers are the observations with the error bars representing uncertainties on the vertical axis, and *JWST* filter profiles indicated in yellow on the horizontal axis. Lower panel: normalized residuals between the observed photometry and the best-fitting model. Right: SEDs across the six *JWST* filters, normalized by the mean flux, for every pixel in the 10×10 pixel region around the transient location (light grey lines). The solid black line is the host-integrated SED, used for SED fitting as described in Section 5.2. The overall SED shape is broadly similar across the host.

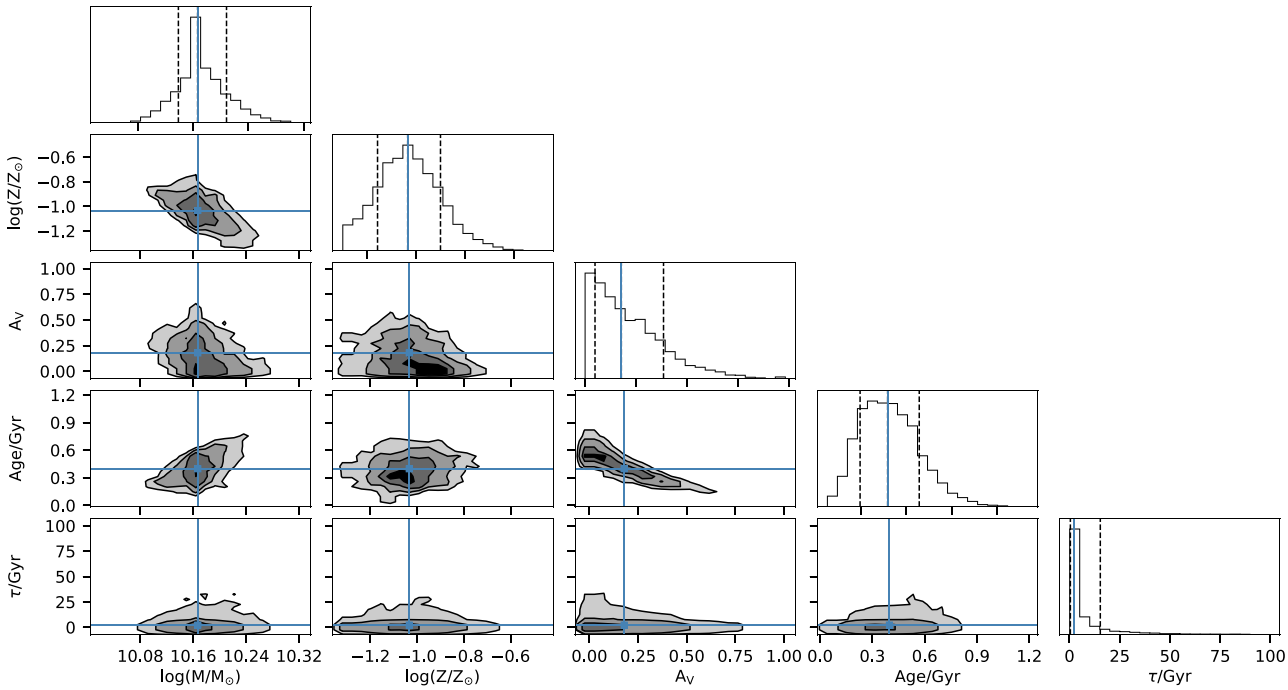

Figure 14. Corner plot for the posterior distribution of the parameters used in the SED fit for the host galaxy of GRB 241105A. This figure was created using the CORNER.PY package (Foreman-Mackey 2016). The best-fitting parameters and their uncertainties are provided in Table 7.

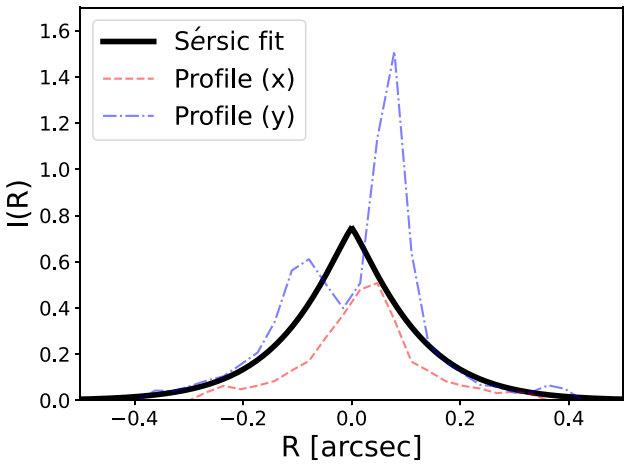

Figure 15. The Sérsic profile fit to the host galaxy, as described in Section 5.3. 1D slices through the host centroid in x and y are also shown.

Nugent et al. (2024). The host has quite high star formation rate as compared to short GRB hosts (see the left panel of Fig. 17). We further included long GRB hosts from Palmerio et al. (2019) and Tanvir et al. (2019). At this stellar mass and redshift, only about 15 per cent of star forming galaxies have similarly high star formation rates (Whitaker et al. 2012), indicating rapidly forming stellar populations. Further, comparison of metallicity with the short GRBs reveals that the host has relatively low metallicity as compared to the short GRBs (see the right panel of Fig. 17). The metallicity is lower (∼0.5 dex) than expected from the mass-star formation rate–metallicity relation (Mannucci et al. 2010; Davé, Finlator & Oppenheimer 2012), consistent with the overall young age. The burst has a small offset from the host centre, and the host's irregular, clumpy morphology, and structural parameters are typical of collapsar hosts. The observed offset of GRB 241105Aa ligns more closely with expectations for collapsar progenitors than for compact object mergers (which generally occur at larger distances due to natal kicks; Narayan, Paczynski & Piran 1992; Bloom, Sigurdsson & Pols 1999; Perna & Belczynski 2002).

We note that another short GRB 090426 ($T_{90} = 1.28$ s and $z = 2.609$), exhibited a host galaxy that was blue, luminous, and actively star-forming with a small angular offset – characteristics more typical of long GRBs from collapsar progenitors (Antonelli et al. 2009), and similar to what we observe for GRB 241105A. However, this is not the case for all high-redshift short bursts; for example, GRB 111117A ($z = 2.211$) had host galaxy properties and an offset from its host centre that are more consistent with merger-driven GRBs (Selsing et al. 2018). These contrasting examples highlight that, while host galaxy properties can offer valuable clues, they alone are not always definitive for distinguishing between progenitor scenarios, especially at high redshift.

7 SUMMARY

We present a comprehensive multiwavelength analysis of GRB 241105A, an ambiguous GRB, exhibiting both short and long GRB characteristics. The key results of our study are summarized below:

(i) The prolonged emission episode of GRB 241105A is spectrally harder than the short, initial pulse. This contrasts with the typical behaviour of extended-emission GRBs from mergers, where the later emission is generally softer than the initial spike.

(ii) Initial emission pulse exhibits a short MVT, aligning with expectations for compact central engines in short GRBs, while the comparatively longer variability time-scale of the later emission episode points to extended activity.

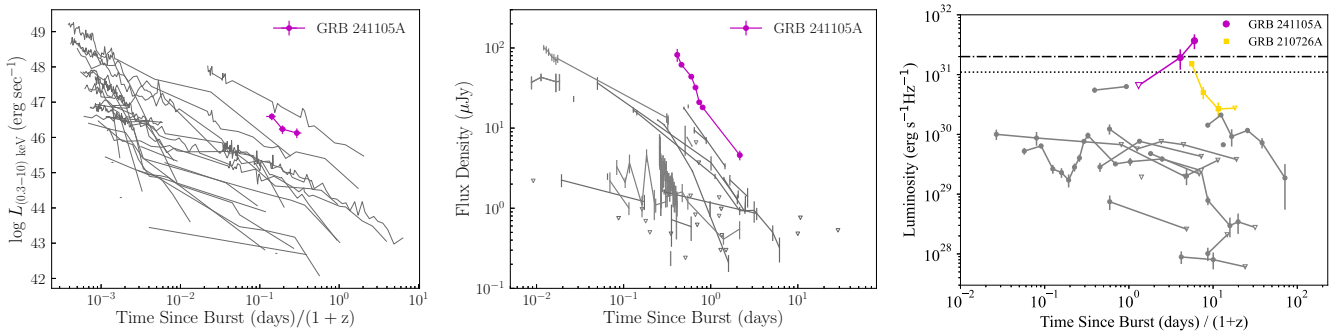

Figure 16. Light curves of short GRBs in the X-ray (0.3–10 keV), optical (*R* band), and radio (8–10 GHz) bands, shown in the left, centre, and right panels, respectively. In all panels, GRB241105A is highlighted in magenta, comparison short GRBs are shown in grey, and open triangles represent 3σ upper limits. GRB 241105A exhibits the brightest optical afterglow among the short GRB population. In the right panel, the dotted line shows the average long GRB luminosity of 1.1×10^{31} erg s^{-1} Hz^{-1} and dot–dashed line shows the mean luminosity between $3 - 6$ d post-burst in the rest frame of $\sim 2 \times 10^{31}$ erg s^{-1} Hz^{-1} (Chandra & Frail 2012).

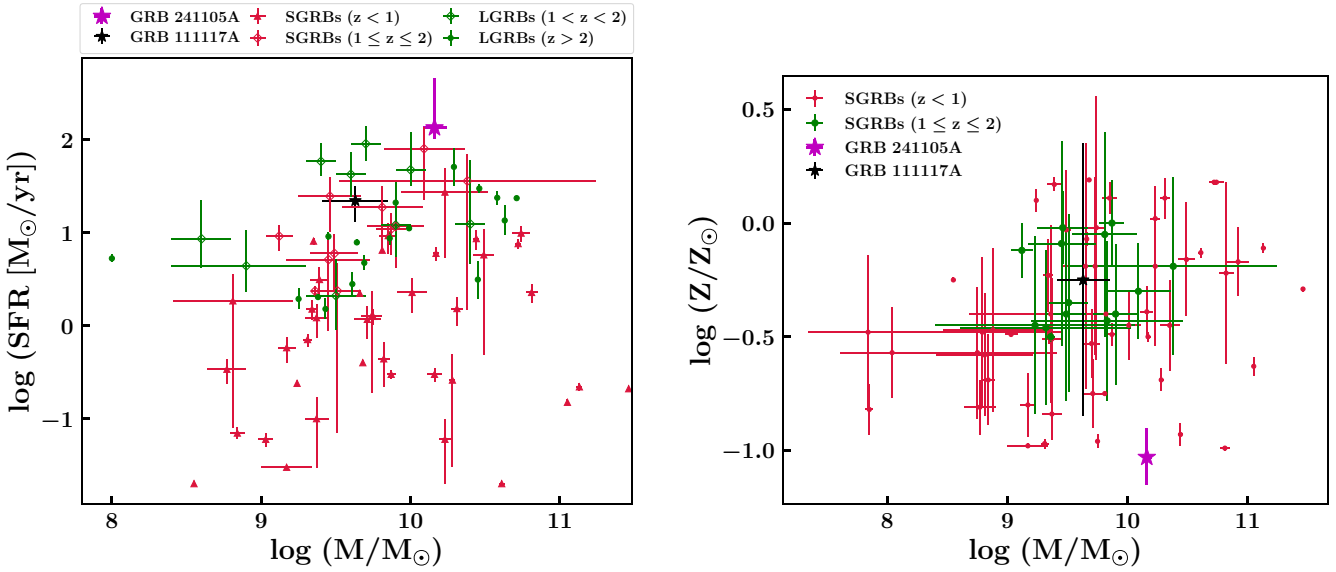

Figure 17. Left: mass versus SFR for GRB 241105A, compared with other short and long GRBs (comparison data compiled from Nugent et al. 2024; Palmerio et al. 2019; Tanvir et al. 2019). Right: *M–Z* relationship for GRB 241105A as compared to other short GRBs compiled from Nugent et al. (2024).

Table 8. Prompt emission properties of GRB 241105A for episode 1, episode 2, and the full burst, as measured from *Swift*/BAT and *Fermi* data.

Instrument	Emission episode	Hardness ratio	MVT (s)	Spectral l ag (ms)
Swift/BAT	Episode 1	1.34 ± 0.17	0.50 ± 0.17	376 ± 11
	Episode 2	1.60 ± 0.25	27.37 ± 0.15	–
	Full Burst	1.58 ± 0.29	–	–
Fermi/GBM	Episode 1	0.856 ± 0.211	0.31 ± 0.09	130.8 ± 230.8
	Episode 2	0.354 ± 0.328	22.58 ± 4.07	–
	Full Burst	0.625 ± 0.034	–	–

(iii) The spectral lag of the initial short pulse is consistent with the lag–luminosity relation, which is usually seen in the case of long GRBs.

(iv) In the Amati plane, the initial short pulse occupies a position near the overlapping region between short and long GRBs. In contrast, the prolonged emission and the whole burst are well located within the short GRB plane.

(v) PCA-UMAP clustering places GRB 241105A near both long collapsars and long-duration mergers, suggesting shared temporal and spectral characteristics with both populations. This proximity suggests shared characteristics, possibly in central engine behaviour (e.g. black hole accretion or magnetar activity) or emission mechanisms (e.g. prolonged jet activity or synchrotron radiation), rather than a definitive progenitor type.

(vi) The afterglow emission is exceptionally luminous in the X-ray, optical, and radio bands compared to the majority of short GRBs. Modelling requires a high-density circumburst medium,

implying a dense, star-forming environment consistent with collapsar progenitors.

(vii) The host galaxy is moderately massive, actively star-forming, and metal-poor, with a star formation rate higher than that observed in typical short GRB hosts. The burst exhibits a small projected offset, which also favours collapsar.

The prompt emission characteristics of GRB 241105A present a complex and non-trivial picture. While the host galaxy properties and the burst environment lend support to a collapsar origin, they do not definitively exclude a compact-binary merger scenario. Notably, the presence of a star-forming environment is not in itself conclusive: GRB 060505, for example, occurred in a vigorously star-forming galaxy, coincided with an H II region showed a spectral lag, yet no SN was detected (Fynbo et al. 2006; McBreen et al. 2008; Xu et al. 2009). Such cases suggest the existence of SN-less collapsars or alternative progenitor channels and caution against relying solely on host galaxy properties for classification.

A compact-binary merger origin remains possible; population simulations of neutron star mergers indicate that merger transients at $z = 2.681$ would have an event probability of $\sim$ 1-in-1000 for *Swift* detected short GRBs, and would likely be well associated with its host galaxy (i.e. have a low impact parameter; Mandhai et al. 2022). Thus, both progenitor scenarios remain viable for GRB 241105A. If this GRB does indeed have a compact-binary merger origin, it would provide observational support for models invoking rapid, early-universe binary evolution and short delay times, which would help to investigate the chemical evolution of the early Universe. On the other hand, if GRB 241105A originated from a collapsar, it may resemble a growing set of high-redshift events that exhibit a bright initial short spike followed by weaker EE. Several such GRBs, identified by Dichiara et al. (2021); Dimple et al. (2022b); and Dimple, Misra & Yadav (2024a), occur in collapsar-like environments, yet mimic the short + EE light-curve morphology. However, in these cases, the EE is detected predominantly in the higher energy bands. GRB 241105A may therefore belong to this ambiguous subset of bursts, suggesting that some similar events might have been misclassified and highlighting the need for a careful re-examination of GRB classification criteria.

GRB 241105A thus sits at the boundary of traditional GRB frameworks, emphasizing the need for more nuanced classification schemes. Whether it marks the most distant compact-binary merger or a rare collapsar with atypical properties, its ambiguous nature makes it a benchmark case for progenitor identification and for probing star formation and chemical enrichment in the early Universe.

ACKNOWLEDGEMENTS

Dimple and BPG acknowledge support from STFC grant no. ST/Y002253/1. BPG and DO acknowledge support from the Leverhulme Trust grant no. RPG-2024-117. Dimple acknowledges Inter University Centre for Astronomy and Astrophysics (IUCAA), India, for their warm hospitality during her stay on the campus. The Gravitational-wave Optical Transient Observer (GOTO) project acknowledges support from the Science and Technology Facilities Council (STFC, grant nos ST/T007184/1, ST/T003103/1, ST/T000406/1, ST/X001121/1, and ST/Z000165/1) and the GOTO consortium institutions; University of Warwick; Monash University; University of Sheffield; University of Leicester; Armagh Observatory & Planetarium; the National Astronomical Research Institute of Thailand (NARIT); University of Manchester; Instituto de Astrofísica de Canarias (IAC); University of Portsmouth; University of Turku. AAC acknowledges support through the European Space Agency (ESA) research fellowship programme. AS acknowledges support by a postdoctoral fellowship from the CNES. AK is supported by the UK Science and Technology Facilities Council (STFC) Consolidated grant ST/V000853/1. TEMB is funded by Horizon Europe ERC grant no. 101125877. KT acknowledges support from the Dynamical Universe, funded by the KAW foundation. SM acknowledges financial support from the Research Council of Finland project 350458. AS acknowledges the Warwick Astrophysics PhD prize scholarship, made possible thanks to a generous philanthropic donation. JDL acknowledges support from a UK Research and Innovation Future Leaders Fellowship (MR/T020784/1). RB acknowledges funding from the Italian Space Agency, contract ASI/INAF n. I/004/11/6. SB, OM, and OR gratefully acknowledge NASA funding from cooperative agreement 80NSSC24M0035. CdB and SMB acknowledge support from funded by Taighde Éireann – Research Ireland under grant nos 21/FFP-A/9043. PV gratefully acknowledges NASA funding from cooperative agreement 80MSFC22M0004. RLCS acknowledges support from The Leverhulme Trust grant no. RPG-2023-240. AR acknowledges support from INAF minigrant 1.05.24.07.04. RB, SC, PDA, AM, and RS acknowledge funding from the Italian Space Agency, contract ASI/INAF n. I/004/11/6. MER is supported by the European Union (ERC, Starstruck, 101095973, PI: Jonker). TLK acknowledges a Warwick Astrophysics prize postdoctoral fellowship made possible thanks to a generous philanthropic donation. IW and MEW are supported by the UKRI Science and Technology Facilities Council (STFC). This work is based [in part] on observations made with the NASA/ESA/CSA *James Webb Space Telescope*. The data were obtained from the Mikulski Archive for Space Telescopes at the Space Telescope Science Institute, which is operated by the Association of Universities for Research in Astronomy, Inc., under NASA contract NAS 5–03127 for *JWST*. These observations are associated with program 9228. We thank the referee for their careful reading of the manuscript and for constructive comments that helped to improve the clarity and quality of this work.

DATA AVAILABILITY

The gamma-ray, X-ray, optical, IR, and radio data sets underlying this article are based on observations collected from public archives and instrument teams, as described in Section 2. *Fermi*/GBM, *Swift*/BAT, *Swift*/XRT, and *Swift*/UVOT data are publicly available from the HEASARC archive.[12] *SVOM*/GRMdata will be made available upon reasonable request from the instrument team. *JWST* data are accessible from the Mikulski Archive for Space Telescopes (MAST)[13] under program ID 9228. Ground-based optical and radio data (including GOTO, VLT/FORS2, NTT, and ATCA) can be obtained from the respective observatories or are available from the corresponding author upon reasonable request.

REFERENCES

Abbott B. P. et al., 2017, ApJ, 848, L13
Acuner Z., Ryde F., 2018, MNRAS, 475, 1708
Ahumada T. et al., 2021, Nat. Astron., 5, 917
Akaike H., 1974, IEEE Trans. Autom. Control, 19, 716

[12] https://heasarc.gsfc.nasa.gov/
[13] https://mast.stsci.edu/

Amati L. et al., 2002, A&A, 390, 81
Amati L., 2006, MNRAS, 372, 233
Anderson et al. 2024c, GCN Circ., 38302, 1
Anderson G. E. et al., 2018, MNRAS, 473, 1512
Anderson G. E. et al., 2024a, ApJ, 975, L13
Anderson G. E. et al., 2024b, GCN Circ., 38189, 1
Antonelli L. A. et al., 2009, A&A, 507, L45
Appenzeller I. et al., 1998, The Messenger, 94, 1
Arnaud K. A., 1996, in Jacoby G. H., Barnes J. eds, ASP Conf. Ser. Vol. 101, Astronomical Data Analysis Software and Systems V, p. 17
Atteia J. L., Cordier B., Wei J., 2022, Int. J. Mod. Phys. D, 31, 2230008
Barthelmy S. D. et al., 2005a, Space Sci. Rev., 120, 143
Barthelmy S. D. et al., 2005b, Nature, 438, 994
Belczynski K., Kalogera V., Bulik T., 2002, ApJ, 572, 407
Belczynski K., Perna R., Bulik T., Kalogera V., Ivanova N., Lamb D. Q., 2006, ApJ, 648, 1110
Belkin S. et al., 2024, MNRAS, 527, 11507
Beniamini P., Piran T., 2019, MNRAS, 487, 4847
Berger E. et al., 2005, Nature, 438, 988
Berger E., Fong W., Chornock R., 2013, ApJ, 774, L23
Bernardini M. G. et al., 2015, MNRAS, 446, 1129
Bissaldi E. et al., 2009, Exp. Astron., 24, 47
Bloom J. S., Sigurdsson S., Pols O. R., 1999, MNRAS, 305, 763
Bradley L. et al., 2024, astropy/photutils: 2.0.2, Zenodo, https://doi.org/10.5281/zenodo.13989456
Breeveld A. A., Landsman W., Holland S. T., Roming P., Kuin N. P. M., Page M. J., 2011, in McEnery J. E., Racusin J. L., Gehrels N.ed., AIP Conf. Ser. Vol. 1358, p. 373,preprint (arXiv:1102.4717)
Bucciantini N., Metzger B. D., Thompson T. A., Quataert E., 2012, MNRAS, 419, 1537
Camisasca A. E. et al., 2023, A&A, 671, A112
Chandra P., Frail D. A., 2012, ApJ, 746, 156
Chastain S. I. et al., 2024, MNRAS, 532, 2820
Chattopadhyay S., Maitra R., 2017, MNRAS, 469, 3374
Cheng L. X., Ma Y. Q., Cheng K. S., Lu T., Zhou Y. Y., 1995, A&A, 300, 746
Chevalier R. A., Li Z.-Y., 2000, ApJ, 536, 195
Conselice C. J. et al., 2005, ApJ, 633, 29
Cordier B. et al., 2015, PoS, SWIFT 10, 005
Côté B. et al., 2019, ApJ, 875, 106
Cupani G., D'Odorico V., Cristiani S., Russo S. A., Calderone G., Taffoni G., 2020, in Proc. SPIE Conf. Ser, p. 114521U
Davé R., Finlator K., Oppenheimer B. D., 2012, MNRAS, 421, 98
de Wet S. et al., 2023, A&A, 677, A32
DeLaunay et al., 2024, GCN Circ., 38091, 1
Desai D., Metzger B. D., Foucart F., 2019, MNRAS, 485, 4404
Dichiara et al., 2024, GCN Circ., 38111, 1
Dichiara S. et al., 2021, ApJ, 911, L28
Dimple et al., 2022a, JA&A, 43, 39
Dimple et al., 2022b, MNRAS, 516, 1
Dimple, Misra K., Arun K. G., 2023, ApJ, 949, L22
Dimple, Misra K., Arun K. G., 2024b, ApJ, 974, 55
Dimple, Misra K., Yadav L., 2024a, Bull. Soc. R. Sci. Liege, 93, 670
Dong Y., Wu B., Li Y., Zhang Y., Zhang S., 2010, Sci. China Phys. Mech. Astron., 53, 40
Dyer M. J. et al., 2020, in Marshall H. K., Spyromilio J., Usuda T., eds, Proc. SPIE Conf. Ser. Vol. 11445, Ground-based and Airborne Telescopes VIII, p. 114457G , preprint (arXiv:2012.02685)
Dyer M. J. et al., 2024, in Marshall H. K., Spyromilio J., Usuda T. eds, Proc. SPIE Conf. Ser. Vol. 13094, Ground-based and Airborne Telescopes X, p. 130941X , preprint (arXiv:2407.17176)
Dyer M. J., 2020, PhD thesis, University of Sheffield, UK
Eldridge J. J., Stanway E. R., Xiao L., McClelland L. A. S., Taylor G., Ng M., Greis S. M. L., Bray J. C., 2017, Publ. Astron. Soc. Aust., 34, e058
Evans P. A. et al., 2007, A&A, 469, 379
Evans P. A. et al., 2009, MNRAS, 397, 1177
Eyles R. A. J. et al., 2019, MNRAS, 489, 13
Fan X. et al., 2020, in Lystrup M., Perrin M. D. eds, Proc. SPIE Conf. Ser. Vol. 11443, Space Telescopes and Instrumentation 2020: Optical, Infrared, and Millimeter Wave, p. 114430Q
Fong W. et al., 2014, ApJ, 780, 118
Fong W. et al., 2021, ApJ, 906, 127
Fong W.-f. et al., 2022, ApJ, 940, 56
Fong W., Berger E., Margutti R., Zauderer B. A., 2015, ApJ, 815, 102
Foreman-Mackey D., 2016, J. Open Source Softw., 1, 24
Foreman-Mackey D., Hogg D. W., Lang D., Goodman J., 2013, PASP, 125, 306
Frederiks et al., 2024, GCN Circ., 38103, 1
Fynbo J. P. U. et al., 2006, Nature, 444, 1047
Fynbo J. P. U. et al., 2009, ApJS, 185, 526
Gal-Yam A. et al., 2006, Nature, 444, 1053
Galama T. J. et al., 1998, Nature, 395, 670
Gehrels N. et al., 2004, ApJ, 611, 1005
Gehrels N. et al., 2006, Nature, 444, 1044
Gillanders J. H. et al., 2023, preprint (arXiv:2308.00633)
Godet O. et al., 2014, in Takahashi T., den Herder J.-W. A., Bautz M. eds, Proc. SPIE Conf. Ser. Vol. 9144, Space Telescopes and Instrumentation 2014: Ultraviolet to Gamma Ray, p. 914424 , preprint (arXiv:1406.7759)
Goldstein A., Cleveland W. H., Kocevski D., 2023, Fermi Gamma-ray Data Tools: v2.0.0, https://github.com/USRA-STI/gdt-fermi
Golkhou V. Z., Butler N. R., Littlejohns O. M., 2015, ApJ, 811, 93
Gompertz B. P. et al., 2018, ApJ, 860, 62
Gompertz B. P. et al., 2023, Nat. Astron., 7, 67
Gompertz B. P., Levan A. J., Tanvir N. R., 2020, ApJ, 895, 58
Gompertz B. P., O'Brien P. T., Wynn G. A., 2014, MNRAS, 438, 240
Gompertz B. P., O'Brien P. T., Wynn G. A., Rowlinson A., 2013, MNRAS, 431, 1745
Goodman J., Narayan R., 2006, ApJ, 636, 510
Gottlieb O. et al., 2023, ApJ, 958, L33
Götz D. et al., 2023, Exp. Astron., 55, 487
Granot J., Sari R., 2002, ApJ, 568, 820
Heintz K. E. et al., 2023, A&A, 679, A91
Hjorth J. et al., 2003, Nature, 423, 847
Hotelling H., 1933, J. Educ. Psychol., 24, 417
Hotokezaka K., Beniamini P., Piran T., 2018, Int. J. Mod. Phys. D, 27, 1842005
Hu et al., 2024, GCN Circ., 38106, 1
Izzo L. et al., 2024, GCN Circ., 38167, 1
Jakobsson P. et al., 2006, A&A, 460, L13
Jeffreys H., 1946, Proc. R. Soc. Lond. A, 186, 453
Jespersen C. K., Severin J. B., Steinhardt C. L., Vinther J., Fynbo J. P. U., Selsing J., Watson D., 2020, ApJ, 896, L20
Jin Z.-P. et al., 2016, Nat. Commun., 7, 12898
Jin Z.-P. et al., 2018, ApJ, 857, 128
Jin Z.-P., Covino S., Liao N.-H., Li X., D'Avanzo P., Fan Y.-Z., Wei D.-M., 2020, Nat. Astron., 4, 77
Jin Z.-P., Li X., Cano Z., Covino S., Fan Y.-Z., Wei D.-M., 2015, ApJ, 811, L22
Johnson B. D., Leja J., Conroy C., Speagle J. S., 2021, ApJS, 254, 22
Julakanti et al., 2024, GCN Circ., 38088, 1
Kaneko Y., Bostancı Z. F., Göğüş E., Lin L., 2015, MNRAS, 452, 824
Kasliwal M. M., Korobkin O., Lau R. M., Wollaeger R., Fryer C. L., 2017, ApJ, 843, L34
Kennea et al., 2024, GCN Circ., 38098, 1
Killestein T. L. et al., 2021, MNRAS, 503, 4838
Kouveliotou C., Meegan C. A., Fishman G. J., Bhat N. P., Briggs M. S., Koshut T. M., Paciesas W. S., Pendleton G. N., 1993, ApJ, 413, L101
Krogager J.-K., 2018, preprint (arXiv:1803.01187)
Lamb G. P. et al., 2019, ApJ, 883, 48

Laskar T. et al., 2013, ApJ, 776, 119
Laskar T. et al., 2014, ApJ, 781, 1
Laskar T. et al., 2016, ApJ, 833, 88
Laskar T. et al., 2022, ApJ, 935, L11
Laskar T., Berger E., Margutti R., Perley D., Zauderer B. A., Sari R., Fong W.-f., 2015, ApJ, 814, 1
Lazzati D., Perna R., Gompertz B. P., Levan A. J., 2023, ApJ, 950, L20
Leja J., Carnall A. C., Johnson B. D., Conroy C., Speagle J. S., van Dokkum P. G., 2019, ApJ, 877, 140
Levan A. J. et al., 2023, Nat. Astron., 7, 976
Levan A. J. et al., 2024, Nature, 626, 737
Lien A. et al., 2016, ApJ, 829, 7
Maccary R. et al., 2025, preprint (arXiv:2508.08995)
MacLachlan G. A. et al., 2013, MNRAS, 432, 857
Mandhai S., Lamb G. P., Tanvir N. R., Bray J., Nixon C. J., Eyles-Ferris R. A. J., Levan A. J., Gompertz B. P., 2022, MNRAS, 514, 2716
Mannucci F., Cresci G., Maiolino R., Marconi A., Gnerucci A., 2010, MNRAS, 408, 2115
McBreen S. et al., 2008, ApJ, 677, L85
McCarthy G. A., Laskar T., 2024, ApJ, 970, 135
McInnes L., Healy J., Melville J., 2018, preprint (arXiv:1802.03426)
Meegan C. et al., 2009, ApJ, 702, 791
Mehta N., Iyyani S., 2024, ApJ, 969, 88
Mei A. et al., 2022, Nature, 612, 236
Metzger B. D., Giannios D., Thompson T. A., Bucciantini N., Quataert E., 2011, MNRAS, 413, 2031
Minaev P. Y., Pozanenko A. S., 2020, MNRAS, 492, 1919
Narayan R., Paczynski B., Piran T., 1992, ApJ, 395, L83
Nasa High Energy Astrophysics Science Archive Research Center (Heasarc), 2014, Astrophysics Source Code Library, record ascl:1408.004
Norris J. P., 2002, ApJ, 579, 386
Norris J. P., Bonnell J. T., 2006, ApJ, 643, 266
Norris J. P., Gehrels N., Scargle J. D., 2010, ApJ, 717, 411
Nugent A. E., Fong W.-f., Castrejon C., Leja J., Zevin M., Ji A. P., 2024, ApJ, 962, 5
O'Connor B. et al., 2021, MNRAS, 502, 1279
O'Shaughnessy R., Belczynski K., Kalogera V., 2008, ApJ, 675, 566
Palmerio J. T. et al., 2019, A&A, 623, A26
Patat F. et al., 2001, ApJ, 555, 900
Patel M. et al., 2023, MNRAS, 523, 4923
Pei Y. C., 1992, ApJ, 395, 130
Peng Z.-Y., Chen J.-M., Mao J., 2024, ApJ, 969, 26
Perley D. A. et al., 2009, ApJ, 696, 1871
Perna R., Belczynski K., 2002, ApJ, 570, 252
Poole T. S. et al., 2008, MNRAS, 383, 627
Prochaska J. X., 2006, ApJ, 650, 272
Proga D., Zhang B., 2006, MNRAS, 370, L61
Qui et al., 2024, GCN Circ., 38099, 1
Rastinejad et al., 2024, GCN Circ., 38113, 1
Rastinejad J. C. et al., 2021, ApJ, 916, 89
Rastinejad J. C. et al., 2022, Nature, 612, 223
Rhoads J. E., 1999, ApJ, 525, 737
Rieke M. J. et al., 2023, PASP, 135, 028001
Rodriguez-Gomez V. et al., 2019, MNRAS, 483, 4140
Roming P. W. A. et al., 2005, Space Sci. Rev., 120, 95
Rossi A. et al., 2022, ApJ, 932, 1
Rosswog S., 2007, MNRAS, 376, L48
Rowlinson A., O'Brien P. T., Metzger B. D., Tanvir N. R., Levan A. J., 2013, MNRAS, 430, 1061
Salmon L., Hanlon L., Martin-Carrillo A., 2022, Galaxies, 10, 78
Sari R., Piran T., Narayan R., 1998, ApJ, 497, L17 +
Sault R. J., Teuben P. J., Wright M. C. H., 1995, in Shaw R. A., Payne H. E., Hayes J. J. E. eds, ASP Conf. Ser. Vol. 77, Astronomical Data Analysis Software and Systems IV, p. 433 , preprint (arXiv:astro-ph/0612759)
Schady P. et al., 2007, MNRAS, 377, 273
Schady P. et al., 2012, A&A, 537, A15
Schlafly E. F., Finkbeiner D. P., 2011, ApJ, 737, 103
Schneider B., Le Floc'h E., Arabsalmani M., Vergani S. D., Palmerio J. T., 2022, A&A, 666, A14
Schroeder G. et al., 2024, ApJ, 970, 139
Schroeder G. et al., 2025a, ApJ, 982, 42
Schroeder G., Fong W., Laskar T., 2025b, GCN Circ., 40545, 1
Schulze S. et al., 2011, A&A, 526, A23
Selsing J. et al., 2018, A&A, 616, A48
Selsing J. et al., 2019, A&A, 623, A92
Shingles L. et al., 2021, Transient Name Server AstroNote, 7, 1
Siegel et al., 2024, GCN Circ., 38110, 1
Skinner D., Wise J. H., 2024, MNRAS, 528, 5825
Smartt S. J. et al., 2015, A&A, 579, A40
Soderberg A. M. et al., 2006, ApJ, 650, 261
Spitzer L., 1998, Physical Processes in the Interstellar Medium
Stanek K. Z. et al., 2003, ApJ, 591, L17
Stanway E. R., Eldridge J. J., 2018, MNRAS, 479, 75
Steeghs D. et al., 2022, MNRAS, 511, 2405
Steinhardt C. L., Mann W. J., Rusakov V., Jespersen C. K., 2023, ApJ, 945, 67
Stratta G. et al., 2025, ApJ, 979, 159
SVOM/GRM Team, 2024, GCN Circ., 38374, 1
Tanvir N. R. et al., 2019, MNRAS, 483, 5380
Tanvir N. R., Levan A. J., Fruchter A. S., Hjorth J., Hounsell R. A., Wiersema K., Tunnicliffe R. L., 2013, Nature, 500, 547
Tauris T. M., Langer N., Moriya T. J., Podsiadlowski P., Yoon S. C., Blinnikov S. I., 2013, ApJ, 778, L23
The Fermi GBM team, 2024, GCN Circ., 38085, 1
Tohuvavohu A., Kennea J. A., DeLaunay J., Palmer D. M., Cenko S. B., Barthelmy S., 2020, ApJ, 900, 35
Tonry J. L. et al., 2018a, PASP, 130, 064505
Tonry J. L. et al., 2018b, ApJ, 867, 105
Troja E. et al., 2018, Nat. Commun., 9, 4089
Troja E. et al., 2019, MNRAS, 489, 2104
Troja E. et al., 2022, Nature, 612, 228
Troja E., King A. R., O'Brien P. T., Lyons N., Cusumano G., 2008, MNRAS, 385, L10
Tsalapatas et al., 2024, GCN Circ., 38119, 1
Ukwatta T. N. et al., 2010, ApJ, 711, 1073
van Dalen J. N. D. et al., 2025, ApJ, 982, L47
van Eerten H. J., Meliani Z., Wijers R. A. M. J., Keppens R., 2011, MNRAS, 410, 2016
Villar V. A. et al., 2017, ApJ, 851, L21
Wei J. et al., 2016, preprint (arXiv:1610.06892)
Wen X. et al., 2021, Nucl. Instrum. Methods Phys. Res. A, 1003, 165301
Whitaker K. E., van Dokkum P. G., Brammer G., Franx M., 2012, ApJ, 754, L29
Xu D. et al., 2009, ApJ, 696, 971
Yang B. et al., 2015, Nat. Commun., 6, 7323
Yang J. et al., 2022, Nature, 612, 232
Yang Y.-H. et al., 2024, Nature, 626, 742
Yi T., Liang E., Qin Y., Lu R., 2006, MNRAS, 367, 1751
Zhang B. B. et al., 2021, Nat. Astron., 5, 911
Zhang B. et al., 2007, ApJ, 655, 989
Zhang B. et al., 2009, ApJ, 703, 1696
Zhang B., 2014, Int. J. Mod. Phys. D, 23, 1430002
Zhang B., Fan Y. Z., Dyks J., Kobayashi S., Mészáros P., Burrows D. N., Nousek J. A., Gehrels N., 2006, ApJ, 642, 354
Zhang B., Mészáros P., 2004, Int. J. Mod. Phys. A, 19, 2385
Zhou H. et al., 2024, GCN Circ., 38124, 1
Zhu J.-P., Wang X. I., Sun H., Yang Y.-P., Li Z., Hu R.-C., Qin Y., Wu S., 2022, ApJ, 936, L10
Zhu S.-Y., Sun W.-P., Ma D.-L., Zhang F.-W., 2024, MNRAS, 532, 1434

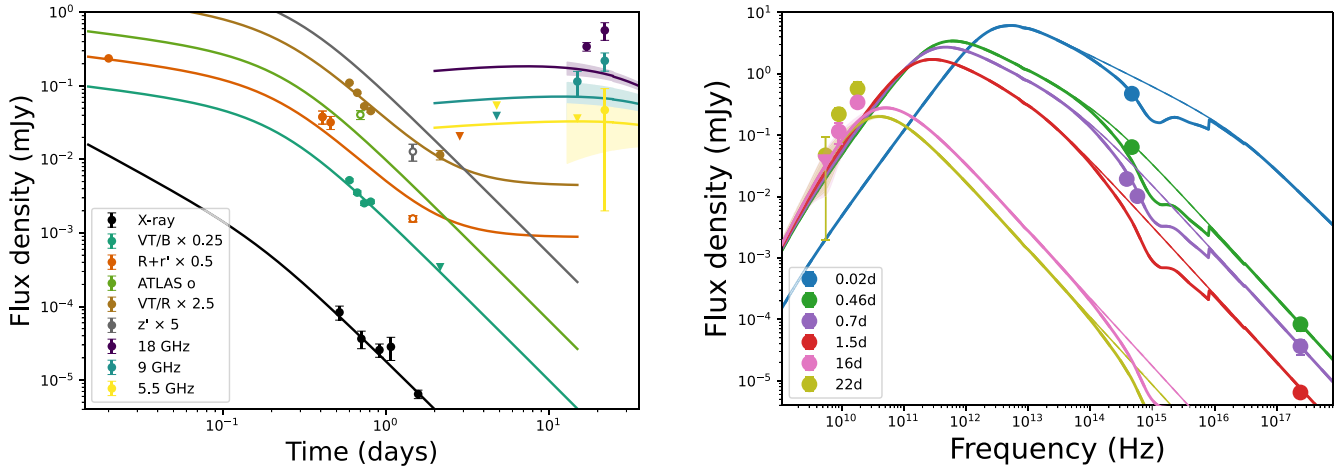

Figure A1. Light curves (left) and SEDs (right) for our best-fitting wind model for the afterglow observations of GRB 241105A. Data points plotted in open symbols are not included in the analysis. Shaded bands indicate 1σ variability at each time expected from interstellar scintillation for reference. The flattening in the VT/R-band and $R + r'$-band light curves is due to a fixed host contribution of 1.8 μJy included in the modelling. Correlation contours for all physical parameters included in the fit, along with the derived parameters of $\theta_{\rm jet}$ and E_K, are presented in Fig. A2 and the corresponding model is discussed in Appendix A. See Fig. 10 for the corresponding light curve and SED plots for the ISM model.

APPENDIX A: WIND MODEL

As discussed in Section 4.3, the observations are degenerate with respect to the circumstellar density profile, and thus both ISM and wind models are feasible. The ISM model is discussed in Section 4.4. In this section, we discuss the wind model. We perform an MCMC analysis identical to that described in Section 4.4. Our best-fitting wind model has $p = 2.21$, $\epsilon_{\rm e} = 0.49$, $\epsilon_{\rm B} = 0.15$, $A_* = 2.5$, $E_{\rm K,iso} = 4.6 \times 10^{52}$ erg, $t_{\rm jet} = 0.17$ d, and $A_V = 0.20$ mag. For these parameters, $\nu_{\rm m} \approx 2.4 \times 10^{15}$ Hz at ≈ 0.1 d, passing through the optical at 0.1–0.4 d, similar to the ISM case. The afterglow is again in fast cooling with $\nu_{\rm c} < \nu_{\rm m}$. The remaining break frequencies for the best-fitting wind model are listed in Table 5. We plot light curves and SEDs from the radio to X-rays of the best-fitting model in Fig. A1 and provide corner plots of the correlations and marginalized posterior density for all fitted parameters (and the derived parameters, $\theta_{\rm jet}$ and E_K) from our MCMC analysis in Fig. A2. We note that the wind model fit results in a slightly poorer $\chi^2_{\rm wind} = 43$ (18 d.o.f.) compared with that for the ISM model ($\chi^2_{\rm ISM} = 41$, 18 d.o.f) due to a marginally poorer fit to the radio data, but the two models are otherwise indistinguishable. We also note that both models result in very similar values for most of the model parameters. The sole exception is ϵ_B, which is, however, strongly degenerate with both the energy and the density (both of which allow for acceptable fits over a range of at least one order of magnitude) due to the unconstrained cooling break. Despite this, the beaming-corrected kinetic energy is consistent at $\log E_{\rm K} \approx 50.3$ between both cases.

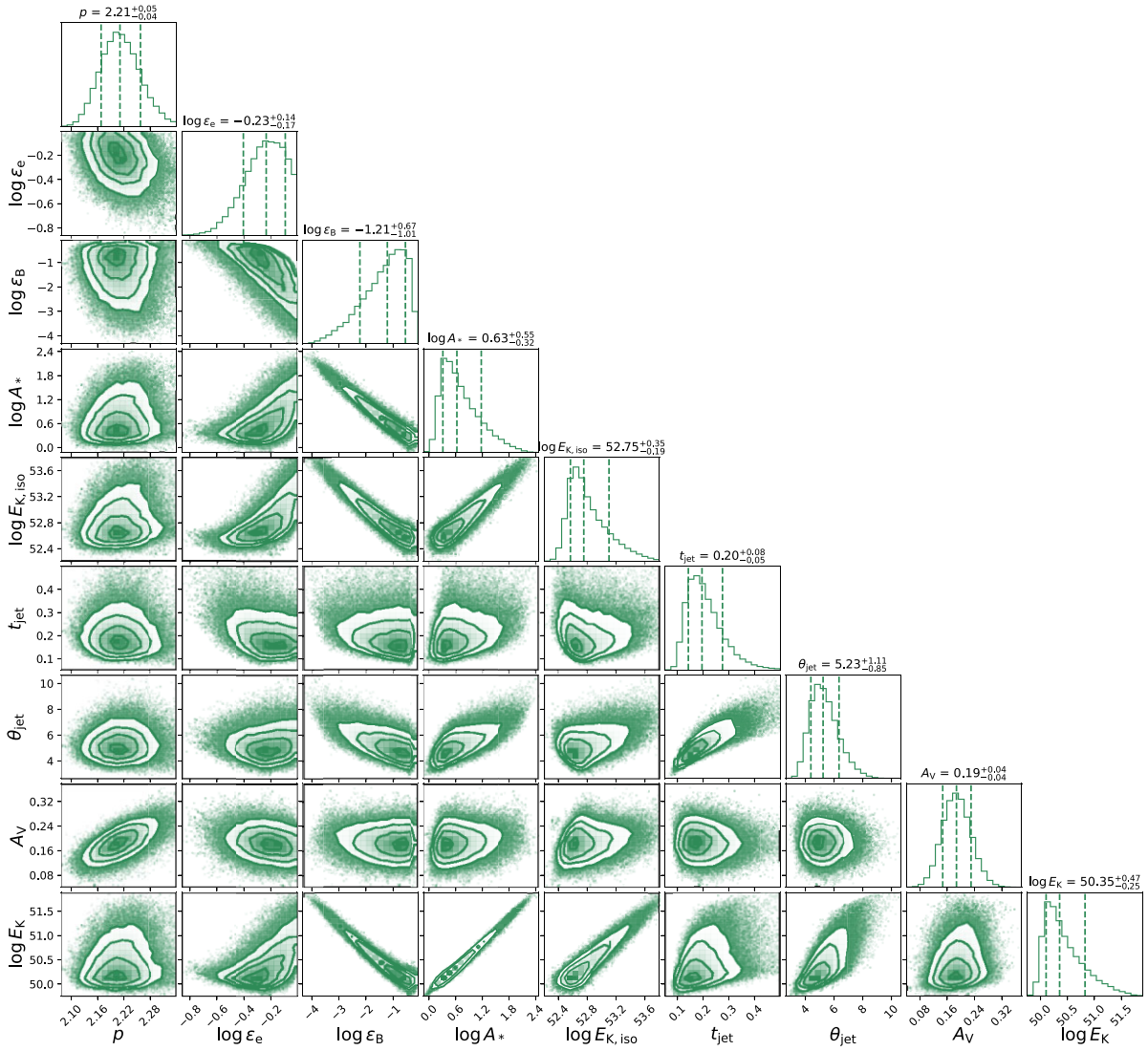

Figure A2. Correlations and marginalized posterior density for all free parameters in the afterglow model in a wind environment. $E_{K,iso}$ and E_K are in units of erg, t_{jet} in days, θ_{jet} in degrees, and A_V in magnitudes. The contours enclose 39.3 per cent, 86.4 per cent, and 98.9 per cent of the probability mass in each correlation plot (corresponding to 1σ, 2σ, and 3σ regions for 2D Gaussian distributions, respectively). The dashed lines indicate the 15.9 per cent, 50 per cent, and 84.1 per cent quantiles, corresponding to the median and $\pm 1\sigma$ for 1D Gaussian distributions. See Fig. 11 for the corresponding corner plot for the ISM model.

APPENDIX B: CURVE OF GROWTH

We conducted the CoG analysis following Spitzer (1998). We identified distinct absorption lines of low-excitation electronic transitions, unblended with other absorption lines or telluric features, to measure the EW of the absorption lines. The Si II 1260,1808 Å lines from the ground state were then used to establish the Doppler parameter, resulting in $b = 112.3 \pm 35.8\,\mathrm{km\,s^{-1}}$, which aligns well with the Voigt fit analysis. A comprehensive explanation of this methodology can be found in the examination of the high-redshift ultralong GRB 220627A (de Wet et al. 2023). Subsequently, we conducted a fit incorporating the entire set of absorption lines listed in Table B1, which exhibit very similar excitation energies, under the assumption that the particles responsible for the absorption features are located in ISM clouds with similar velocity distributions (same b parameter). Although higher excitation features were detected in the spectrum of GRB 241105A, only Si IV 1393,1404 Å were not blended with other features, so we skip the CoG analysis for these high-excitation lines. The findings of our analysis are presented in Table B1 and Fig. B1. Moreover, it is worth noting that the relatively high column density of C II 1334 Å is likely influenced by the presence of an underlying C II* transition, which enhances the EW measured for this line and the corresponding column density. It is important to remark that the majority of the absorption features in this analysis fall in the flat/saturated regime of the CoG, indicating that the column densities obtained through this methodology should be approached with caution and considered as lower limits to the actual density of absorbers in the ISM clouds (Prochaska 2006). The low spectral resolution of FORS2 primarily drives this conclusion. At an average resolving power of $R = 440$ (grism 300V) and $R = 660$ (grism 300I), the dispersion velocity resolution measured is approximately $\delta v \approx 550\,\mathrm{km\,s^{-1}}$ at 6655 Å, which corresponds to the observed wavelength of Si II 1808 Å. This implies that we cannot resolve individual ISM clouds, particularly those located in the immediate

Table B1. Column densities derived via the CoG method for various ionic transitions. EWs and observed wavelengths are reported alongside their respective column densities, with uncertainties reflecting 1σ confidence intervals.

Ion	λ_{obs} (Å)	EW$_\lambda$ (Å)	log N_X
Si II 1260	4639.6	6.74 ± 3.17	$15.90^{+0.53}_{-0.53}$
Si II 1527	5619.8	7.93 ± 3.01	$15.90^{+0.53}_{-0.53}$
Si II 1808	6655.3	2.55 ± 0.73	$15.90^{+0.53}_{-0.53}$
C II 1334	4912.4	9.93 ± 3.18	$16.84^{+0.80}_{-1.00}$
Si II* 1533	5644.6	1.30 ± 0.44	$14.10^{+0.18}_{-0.27}$
Fe II 1608	5920.7	3.99 ± 1.31	$15.43^{+0.32}_{-0.31}$
Fe II 2344	8629.0	10.22 ± 3.95	$15.43^{+0.32}_{-0.31}$
Fe II 2374	8740.4	8.22 ± 2.65	$15.43^{+0.32}_{-0.31}$
Fe II 2383	8770.9	7.23 ± 4.12	$15.43^{+0.32}_{-0.31}$
Fe II 2587	9521.4	10.21 ± 3.60	$15.43^{+0.32}_{-0.31}$
Fe II 2600	9571.2	15.98 ± 6.25	$15.43^{+0.32}_{-0.31}$
Al II 1671	6150.2	10.01 ± 3.22	$15.55^{+1.26}_{-1.07}$

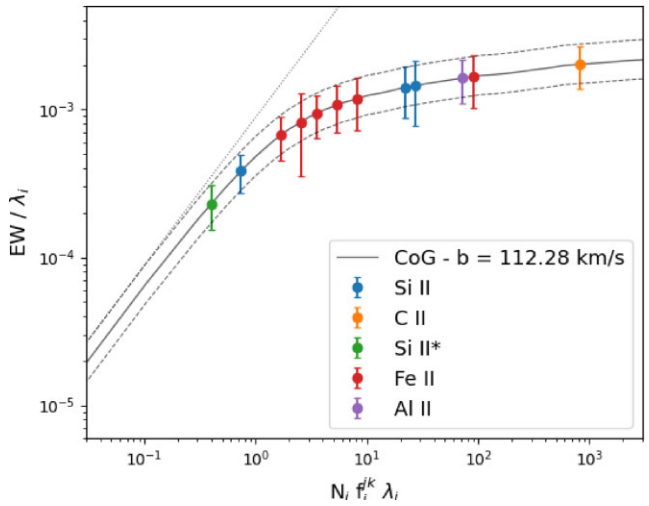

Figure B1. The results of the CoG analysis. Absorption lines from the same ionized state have been reported with the same colour. Confidence limits, dashed lines, have been provided at 2σ level. The dotted line corresponds to the linear case, where lines are not considered saturated.

vicinity of the GRB. Therefore, each absorption line in this analysis involves contributions from multiple, if not all, clouds within the GRB host galaxy, reinforcing the notion that our measurements should be considered lower limits. Furthermore, we did not perform a more detailed metallicity and dust depletion analysis of the ISM given these limitations.

[1]*School of Physics and Astronomy, University of Birmingham, Edgbaston, Birmingham B15 2TT, UK*
[2]*Institute for Gravitational Wave Astronomy, University of Birmingham, Birmingham B15 2TT, UK*
[3]*Department of Astrophysics/IMAPP, Radboud University, NL-6525 AJ Nijmegen, The Netherlands*
[4]*Department of Physics & Astronomy, University of Utah, Salt Lake City, UT 84112, USA*
[5]*Science and Technology Institute, Universities Space Research Association, Huntsville, AL 35805, USA*
[6]*European Space Agency (ESA), European Space Research and Technology Centre (ESTEC), Keplerlaan 1, NL-2201 AZ Noordwijk, The Netherlands*
[7]*Niels Bohr Institute, University of Copenhagen, Jagtvej 128, DK-2200 Copenhagen N, Denmark*
[8]*INAF, Osservatorio Astronomico di Capodimonte, Salita Moiariello 16, I-80131, Naples, Italy*
[9]*Astrophysics Research Institute, Liverpool John Moores University, IC2 Liverpool Science Park, 146 Brownlow Hill, Liverpool L3 5RF, UK*
[10]*Université Paris-Saclay, Université Paris Cité, CEA, CNRS, AIM, F-91191, Gif-sur-Yvette, France*
[11]*International Centre for Radio Astronomy Research, Curtin University, GPO Box U1987, Perth, WA 6845, Australia*
[12]*School of Physics, Centre for Space Research, Science Center North, University College Dublin, Dublin 4, D04 V1W8, Ireland*
[13]*State Key Laboratory of Particle Astrophysics, Institute of High Energy Physics, Chinese Academy of Sciences, Beijing 100049, China*
[14]*Department of Physics, Royal Holloway – University of London, Egham Hill, Egham TW20 0EX, UK*
[15]*Key Laboratory of Space Astronomy and Technology, National Astronomical Observatories, Chinese Academy of Sciences, Beijing 100101, China*
[16]*Department of Physics, Lancaster University, Lancaster LA1 4YB, UK*
[17]*Department of Physics, Indian Institute of Technology Bombay, Powai, Mumbai 400076, India*
[18]*School of Physics, Indian Institute of Science Education and Research Thiruvananthapuram, Thiruvananthapuram 695551, India*
[19]*Centre for High Performance Computing, Indian Institute of Science Education and Research Thiruvananthapuram, Thiruvananthapuram 695551, India*
[20]*Department of Space Science and Center for Space Plasma and Aeronomic Research, University of Alabama in Huntsville, Huntsville, AL 35899, USA*
[21]*Department of Physics, University of Warwick, Coventry CV4 7AL, UK*
[22]*INAF, Osservatorio Astronomico di Brera, Via E. Bianchi 46, I-23807 Merate (LC), Italy*
[23]*INAF – Osservatorio di Astrofisica e Scienza dello Spazio, via Piero Gobetti 93/3, I-40024 Bologna, Italy*
[24]*School of Physics and Astronomy, University of Leicester, University Road, LE1 7RH Leicester, UK*
[25]*European Southern Observatory, Alonso de Córdova 3107, Casilla 19, Santiago, 19001, Chile*
[26]*Millennium Institute of Astrophysics MAS, Nuncio Monsenor Sotero Sanz 100, Off. 104, Providencia, Santiago, 19001, Chile*
[27]*Excellence Cluster ORIGINS, Boltzmannstraße 2, D-85748 Garching, Germany*
[28]*Ludwig-Maximilians-Universität, Schellingstraße 4, D-80799 München, Germany*
[29]*School of Physics and Astronomy, Monash University, Clayton, VIC 3800, Australia*
[30]*Jodrell Bank Centre for Astrophysics, University of Manchester, Manchester M13 9PL, UK*
[31]*Department of Physics & Astronomy, Louisiana State University, Baton Rouge, LA 70803, USA*
[32]*Instituto de Astrofísica de Canarias, E-38205 La Laguna, Tenerife, Spain*
[33]*Departamento de Astrofísica, Universidad de La Laguna, E-38206 La Laguna, Tenerife, Spain*
[34]*Department of Physics and Astronomy, University of New Mexico, 210 Yale Blvd NE, Albuquerque, NM 87106, USA*
[35]*Space Science Data Center (SSDC) – Agenzia Spaziale Italiana (ASI), I-00133 Roma, Italy*
[36]*School of Mathematical and Physical Sciences, University of Sheffield, Sheffield S3 7RH, UK*
[37]*Sydney Institute for Astronomy, School of Physics, The University of Sydney, NSW 2006, Australia*
[38]*ARC Centre of Excellence for Gravitational Wave Discovery (OzGrav), Hawthorn, VIC 3122, Australia*
[39]*CSIRO Space and Astronomy, PO Box 76, Epping, NSW 1710, Australia*
[40]*Astronomical Observatory, University of Warsaw, Al. Ujazdowskie 4, PL-00-478 Warszawa, Poland*
[41]*Department of Physics and Astronomy, Clemson University, Clemson, SC 29634, USA*

[42]*Center for Astrophysics and Cosmology, Science Institute, University of Iceland, Dunhagi 5, 107 Reykjavik, Iceland*
[43]*Department of Physics and Astronomy, University of Turku, FI-20014 Turku, Finland*
[44]*David A. Dunlap Department of Astronomy and Astrophysics, University of Toronto, 50 St. George Street, Toronto, ON M5S 3H4, Canada*
[45]*Dunlap Institute for Astronomy and Astrophysics, University of Toronto, 50 St. George Street, Toronto, ON M5S 3H4, Canada*
[46]*Racah Institute of Physics, The Hebrew University of Jerusalem, Jerusalem 91904, Israel*
[47]*INAF, Osservatorio Astronomico di Roma, via Frascati 33, I-00078 Monte Porzio Catone (Roma), Italy*
[48]*School of Sciences, European University Cyprus, Diogenes Street, Engomi, 1516 Nicosia, Cyprus*
[49]*School of Mathematical and Physical Sciences, Macquarie University, NSW 2109, Australia*
[50]*Astrophysics and Space Technologies Research Centre, Macquarie University, Sydney, NSW 2109, Australia*
[51]*School of Physics, Trinity College Dublin, The University of Dublin, Dublin 2, Ireland*
[52]*Instituto de Ciencias Exactas y Naturales (ICEN), Universidad Arturo Prat, Chile*
[53]*National Astronomical Research Institute of Thailand (NARIT), Chiang Mai 50180, Thailand*
[54]*Institute of Cosmology and Gravitation, University of Portsmouth, Portsmouth PO1 3FX, UK*
[55]*Department of Mathematics and Computer Sciences, Physical Sciences and Earth Sciences, University of Messina, F.S. D'Alcontres 31, I-98166 Messina, Italy*
[56]*Instituto de Alta Investigación, Universidad de Tarapacá, Casilla 7D, Arica, Chile*
[57]*Anton Pannekoek Institute of Astronomy, University of Amsterdam, Science Park 904, NL-1098 XH Amsterdam, The Netherlands*
[58]*Armagh Observatory & Planetarium, College Hill, Armagh BT61 9DB, UK*
[59]*INAF – Istituto di Astrofisica Spaziale e Fisica Cosmica di Milano, Via A. Corti 12, I-20133 Milano, Italy*
[60]*Department of Physics, University of Bath, Claverton Down, Bath BA2 7AY, UK*
[61]*Aix Marseille University, CNRS, CNES, LAM, Marseille, France*
[62]*The Oskar Klein Centre, Department of Astronomy, Stockholm University, AlbaNova, SE-10691, Stockholm, Sweden*
[63]*Department of Physics, George Washington University, 725 21st St NW, Washington, DC 20052, USA*
[64]*University of Chinese Academy of Sciences, Chinese Academy of Sciences, Beijing 100049, China*
[65]*Centre for Astrophysics Research, University of Hertfordshire, College Lane, Hatfield AL10 9AB, UK*

This paper has been typeset from a TEX/LATEX file prepared by the author.